Monthly Notices
of the
ROYAL ASTRONOMICAL SOCIETY

MNRAS **521,** 5453–5472 (2023) https://doi.org/10.1093/mnras/stad887
Advance Access publication 2023 March 23

The multiwavelength view of shocks in the fastest nova V1674 Her

K. V. Sokolovsky,[1,2]★ T. J. Johnson,[3]† S. Buson,[4] P. Jean,[5,6] C. C. Cheung,[7] K. Mukai,[8] L. Chomiuk,[2] E. Aydi,[2] B. Molina,[2] A. Kawash,[2] J. D. Linford,[9] A. J. Mioduszewski,[9] M. P. Rupen,[10] J. L. Sokoloski,[11] M. N. Williams,[9] E. Steinberg,[12] I. Vurm,[13] B. D. Metzger,[11,14] K. L. Page,[15] M. Orio,[16,17] R. M. Quimby,[18,19] A. W. Shafter,[18] H. Corbett,[20] S. Bolzoni,[21,22] J. DeYoung,[21] K. Menzies,[21] F. D. Romanov,[21,22] M. Richmond,[23] J. Ulowetz,[24] T. Vanmunster,[21,25,26] G. Williamson,[21] D. J. Lane,[27,21] M. Bartnik,[2] M. Bellaver,[2] E. Bruinsma,[2] E. Dugan,[2] J. Fedewa,[2] C. Gerhard,[2] S. Painter,[2] D.-M. Peterson,[2] J. E. Rodriguez,[2] C. Smith,[2] H. Sullivan[2] and S. Watson[2]

Affiliations are listed at the end of the paper

Accepted 2023 March 14. in original form 2023 February 3

ABSTRACT

Classical novae are shock-powered multiwavelength transients triggered by a thermonuclear runaway on an accreting white dwarf. V1674 Her is the fastest nova ever recorded (time to declined by two magnitudes is $t_2 = 1.1$ d) that challenges our understanding of shock formation in novae. We investigate the physical mechanisms behind nova emission from GeV γ-rays to cm-band radio using coordinated *Fermi*-LAT, *NuSTAR*, *Swift*, and VLA observations supported by optical photometry. *Fermi*-LAT detected short-lived (18 h) 0.1–100 GeV emission from V1674 Her that appeared 6 h after the eruption began; this was at a level of $(1.6 \pm 0.4) \times 10^{-6}$ photons cm^{-2} s^{-1}. Eleven days later, simultaneous *NuSTAR* and *Swift* X-ray observations revealed optically thin thermal plasma shock-heated to $kT_{\rm shock} = 4$ keV. The lack of a detectable 6.7 keV Fe Kα emission suggests super-solar CNO abundances. The radio emission from V1674 Her was consistent with thermal emission at early times and synchrotron at late times. The radio spectrum steeply rising with frequency may be a result of either free-free absorption of synchrotron and thermal emission by unshocked outer regions of the nova shell or the Razin–Tsytovich effect attenuating synchrotron emission in dense plasma. The development of the shock inside the ejecta is unaffected by the extraordinarily rapid evolution and the intermediate polar host of this nova.

Key words: stars: individual: V1674 Her – novae, cataclysmic variables – white dwarfs – transients: novae.

1 INTRODUCTION

Novae are multiwavelength transients powered by a sudden ignition of thermonuclear fusion at the bottom of a hydrogen-rich shell accreted by a white dwarf from its binary companion (e.g. Bode & Evans 2008; Starrfield, Iliadis & Hix 2016; Della Valle & Izzo 2020; Starrfield et al. 2020). The ignition leads to a dramatic expansion and ejection of the white dwarf atmosphere at typical velocities of ~500–5000 km s^{-1} – a hallmark feature of the nova phenomenon recognized since the earliest days of spectroscopy (Pickering 1895; McLaughlin 1956; Aydi et al. 2020b). The expanded atmosphere leads to a dramatic, albeit temporary, increase in the optical brightness of the host binary system by ~8–15 mag (Vogt 1990; Warner 2008; Kawash et al. 2021), reaching absolute magnitudes of −4 to −10 mag (Shafter et al. 2009; Shafter 2017; Schaefer 2022). While the optical continuum light of a nova fades on a time-scale of days to months, the warm ejected envelope remains the source of optical line and radio continuum emission for months and years after the eruption (Strope, Schaefer & Henden 2010; Chomiuk et al. 2021b). About 30 such events occur in the Galaxy each year, with only 10 events per year typically observed while others remain hidden by dust extinction (Shafter 2017; De et al. 2021; Kawash et al. 2022; Rector et al. 2022).

Novae are prominent sources of X-rays. As the eruption progresses, a nova goes through the following phases of X-ray light-curve development (Hernanz & Sala 2010; Mukai 2017):

(i) ‘fireball’ phase – a bright soft (<0.1 keV) thermal X-ray flash seen hours before the optical rise (Kato, Saio & Hachisu 2022; König et al. 2022);

(ii) shock-dominated phase – hard (~1–10 keV) thermal X-ray emission of plasma heated by shocks within the nova ejecta (O’Brien, Lloyd & Bode 1994; Metzger et al. 2014; Mukai et al. 2014; Orio et al. 2020; Gordon et al. 2021);

(iii) super-soft (<0.5 keV, SSS) thermal X-rays that appear when the ejecta clears, revealing the white dwarf heated by the ongoing thermonuclear reactions (Schwarz et al. 2011; Ness et al. 2013; Orio et al. 2018);

(iv) accretion-powered hard (typically >1 keV) X-rays produced by shocked plasma at the interface between the stream of accreting material and the white dwarf surface – similar to non-nova accreting white dwarf binaries (Balman 2020; de Martino et al. 2020; Sun et al. 2020).

★ E-mail: kirx@kirx.net
† Resident at: Naval Research Laboratory, Washington, DC 20375, USA.

Published by Oxford University Press on behalf of Royal Astronomical Society

The discovery that shocks are playing an essential role in energy transport within the nova shell has led to a renewed interest in novae (for a recent review see Chomiuk, Metzger & Shen 2021a). The role of shocks was revealed by the initial detection of continuum GeV γ-ray emission from novae with *Fermi*-LAT (Abdo et al. 2010; Ackermann et al. 2014), followed by observations of shocks contributing to nova optical light (Li et al. 2017; Aydi et al. 2020a) and recent very high-energy (TeV) detections of the recurrent nova RS Oph (Acciari et al. 2022; Cheung et al. 2022; H. E. S. S. Collaboration 2022).

Novae can serve as laboratories for studying astrophysical shocks, which may power the emission of diverse transients (Fang et al. 2020) including Type IIn and super-luminous supernovae (e.g. Ofek et al. 2014; Chandra 2018), tidal disruption events (Piran et al. 2015), stellar mergers or 'Luminous Red Novae' (Metzger & Pejcha 2017), and neutron star mergers (Lee, Maeda & Kawanaka 2018). Understanding particle acceleration efficiency at shocks (Caprioli & Spitkovsky 2014; Steinberg & Metzger 2018) and the prospects of detecting neutrinos from a nearby (∼1 kpc) nova eruption are also of interest (Razzaque, Jean & Mena 2010; Metzger et al. 2016; Fang et al. 2020; Abbasi et al. 2022; Guetta, Hillman & Della Valle 2023). Finally, as the nova envelope swells to encompass the binary star, it may remain marginally bound to the system (e.g. Pejcha, Metzger & Tomida 2016). Thus, each nova eruption serves as a test of common envelope evolution (Shankar, Livio & Truran 1991; Sparks & Sion 2021) – a poorly understood evolutionary stage passed by all interacting binaries (Paczynski 1976; Livio & Soker 1988; Ritter 2010; Ivanova et al. 2013). The angular momentum loss during nova eruption may be the key to understanding white dwarf binaries evolution (Schenker, Kolb & Ritter 1998; Schreiber, Zorotovic & Wijnen 2016; Metzger et al. 2021; Pala et al. 2022).

Multiple physical mechanisms, including hydrodynamic pressure supported by heat from nuclear reactions (Sparks 1969; Starrfield, Truran & Sparks 1978; Prialnik 1986), radiation pressure (Bath & Shaviv 1976; Sparks, Starrfield & Truran 1978; Kato & Hachisu 1994; Shaviv 2001), and interactions with a binary companion (MacDonald, Fujimoto & Truran 1985; Livio 1990; Livio et al. 1990), have long been recognized as potential causes of envelope ejection in novae. The 'slow torus – fast bipolar wind' scenario of nova eruption outlined by Livio (1990), Chomiuk et al. (2014, 2021a), Mukai & Sokoloski (2019), and Shen & Quataert (2022) can be summarized as follows. Thermonuclear reactions heat the white dwarf atmosphere that expands engulfing the binary. Little (if any) material is ejected as the result of the sudden explosive onset of the nuclear burning. The weight of the expanded atmosphere would prevent the formation of fast radiation-driven wind from the white dwarf until most of the atmosphere is ejected via the common envelope interaction. The velocity of the wind is expected to be close to the escape velocity at the distance from the white dwarf centre where the wind forms. Without a close companion that would disrupt the expanded atmosphere, the wind would launch farther away from the white dwarf's centre and at a slower speed (Shen & Quataert 2022). The ejected common envelope produces the slow equatorial flow – the presumed target for the fast white dwarf wind to shock. We put this scenario to the test with the observations of V1674 Her.

We examine observations of V1674 Her in the GeV γ-ray (0.1–300 GeV from *Fermi*-LAT; Section 3.3), hard (3–78 keV from *NuSTAR*; Section 3.1), and soft X-ray (0.3–10 keV from *Swift*/XRT), and ultraviolet (*Swift*/UVOT; Section 3.2), as well as radio (Karl G. Jansky Very Large Array – VLA; Section 3.4) bands, putting them in the context of its optical light curve. In Section 4, we discuss how the observed high-energy and radio behaviour results from shock waves mediating energy transport within the expanding nova shell and compare V1674 Her to other novae, specifically the ones previously observed by *NuSTAR*. We make concluding remarks in Section 5.

Throughout this paper we report uncertainties at the 1σ level, unless stated otherwise. For hypothesis testing, we adopt a significance level $\alpha_{\rm lim} = 0.05$ (the probability of rejecting the null hypothesis when it is true), which is equivalent to the confidence level $(1 - \alpha_{\rm lim}) = 0.95$ (or 2σ). Note, that when reporting p-values in relation to the variability and periodicity detection in Sections 3.1.1, 3.2, and 3.3 the null hypothesis is the absence of the effect ($p > \alpha_{\rm lim}$ means non-detection), while in the X-ray spectral fitting discussion (Sections 3.1.2 and 3.2) we follow the XSPEC (Arnaud 1996) convention of the null hypothesis being that 'the adopted spectral model is true' ($p > \alpha_{\rm lim}$ means we have a good model). For power law spectra, we use the positively defined spectral index α: $F_\nu \propto \nu^\alpha$ where F_ν is the flux density and ν is the frequency; the corresponding index in the distribution of the number of photons as a function of energy is $\mathrm{d}N(E)/\mathrm{d}E \propto E^{-\Gamma}$, where Γ is the photon index and $\Gamma = 1 - \alpha$. The same power law expressed in spectral energy distribution units (SED; Gehrels 1997) is $\nu F_\nu \propto \nu^{\alpha+1} \propto \nu^{-\Gamma+2}$.

2 V1674 HER – NOVA HERCULIS 2021

The eruption of V1674 Her (also known as Nova Herculis 2021, TCP J18573095+1653396, ZTF19aasfsjq) was discovered on 2021-06-12.5484 UTC by Seiji Ueda and reported via the Central Bureau for Astronomical Telegrams' Transient Objects Confirmation Page[1] (Kazarovets et al. 2021; Ueda et al. 2021). The transient was spectroscopically confirmed as a classical nova by Munari, Valisa & Dallaporta (2021), Aydi et al. (2021), and Ueda et al. (2021). The All-Sky Automated Survey for Supernovae (ASAS-SN; Shappee et al. 2014; Kochanek et al. 2017) detected V1674 Her on 2021-06-12.1903 (8.4 h before discovery) at $g = 16.62$. The final pre-eruption ASAS-SN observation of the field without a detection was on 2021-06-10.9660, which places the start of the eruption between these two dates. Throughout this paper we adopt the date of the first ASAS-SN detection (the first available observation of V1674 Her above the quiescence level) as the eruption start time t_0 = JD(UTC)2459377.6903.

Quimby, Shafter & Corbett (2021) report photometry of V1674 Her on the rise to maximum light using Evryscope (g band; Law et al. 2014) and the Mount Laguna Observatory All-Sky Camera (MLO-ASC; an unfiltered monochrome camera based on a blue-sensitive Panasonic MN34230 CMOS chip) that is normally used for cloud cover monitoring. Quimby et al. (2021) used a custom code based on ASTROPY and PHOTUTILS to perform photometry on the MLO-ASC images that was calibrated using *Gaia G* magnitudes of nearby field stars. The MLO-ASC data cover the near-peak time when the nova was saturated for Evryscope. We reproduce these observations in Fig. 1, combining them with ASAS-SN (g band; Shappee et al. 2014; Kochanek et al. 2017) data, as well as V band and CV (unfiltered observations with V magnitude zero-point) photometry and visual brightness estimates collected by the AAVSO observers (Kafka 2021).

The light curve of V1674 Her is presented at Fig. 1. The nova experienced a pre-maximum halt at $g \sim 14$ lasting for at least three hours (Quimby et al. 2021). The halt was followed by a

---

[1] http://www.cbat.eps.harvard.edu/unconf/followups/J18573095 + 1653396.html

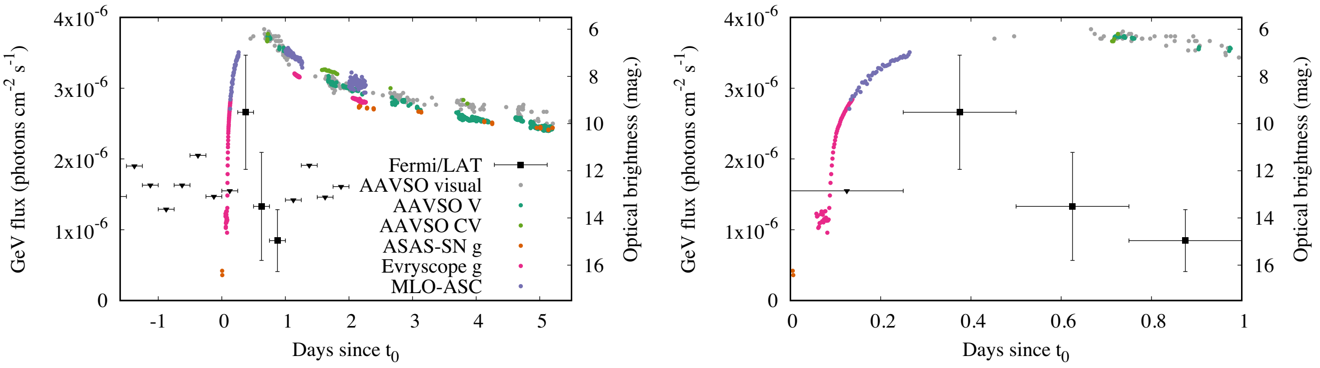

Figure 1. The optical and γ-ray light curves of V1674 Her. The *Fermi*-LAT detections are shown as black squares while the 95 per cent upper limits are marked with black triangles. The left-hand panel shows the full duration of the *Fermi*-LAT 6 h binned light curve. The right-hand panel zooms into the first day of the eruption.

steep rise to the peak around the visual magnitude of 6 on 2021-06-12.856 according to the AAVSO photometry (Kafka 2021) and the measurements reported by Ueda et al. (2021) and Kazarovets et al. (2021). V1674 Her rapidly declined from the peak, fading by two magnitudes (t_2) in 1.1 (Quimby et al. 2021) or 1.2 d (Shugarov & Afonina 2021) making it one of the fastest novae ever observed (Woodward et al. 2021; Woodward, Wagner & Starrfield 2022). The colour of novae near peak brightness changes rapidly (due to changing photospheric temperature and development of emission lines; van den Bergh & Younger 1987), resulting in slight differences in decline rates between the bands. The uncertainty in the maximum light epoch and magnitude may have also contributed to the difference between the reported t_2 estimates for V1674 Her. Regardless of the exact value of t_2, V1674 Her is clearly among the fastest novae observed, leading its nearest competitors U Sco ($t_2 =$ 1.2 d; Schaefer 2010), V838 Her (Strope et al. 2010 report $t_2 = 1$ d whereas Vanlandingham et al. 1996 quote $t_2 \sim 2$ d), M31N 2008-12a ($t_2 = 1.6$ d; Darnley et al. 2016), V1500 Cyg ($t_2 = 2$ d), V4160 Sgr ($t_2 = 2$ d), V4739 Sgr ($t_2 = 2$ d; Strope et al. 2010), and V392 Per ($t_2 = 2$ d; Murphy-Glaysher et al. 2022); see also table 5 of Darnley et al. (2016).

Spectroscopic observations revealed shell expansion velocities that are some of the fastest observed in novae. Munari et al. (2021) report P Cygni profiles of Balmer and Fe II with absorption troughs blueshifted by 3000 km s^{-1} less than a day after the discovery. Aydi et al. (2021) noted dramatic changes in the line profiles over the course of a day – in addition to the initial 3000 km s^{-1} absorption components, faster components (P Cygni absorptions with troughs at blueshifted velocities >5000 km s^{-1}) appeared in less than a day. Aydi et al. (2021) interpreted these two velocity components in the context of multiple outflows described in Aydi et al. (2020b). NIR spectroscopic observations were reported by Woodward et al. (2021) showing the emergence of coronal lines as early as t_0 + 11 d, the earliest onset yet observed for any classical nova. Based on late time optical spectroscopic follow up taken more than 300 days after eruption, Woodward et al. (2022) suggested that the eruption is over. They also report P Cygni-like profile of Hα, suggesting the presence of a wind emanating from the binary system.

GeV γ-ray emission from V1674 Her was detected by *Fermi*-LAT as reported by Li (2021a, b); Lin et al. (2022), see Section 3.3 for our independent analysis. Along with the dedicated X-ray observations (Drake et al. 2021; Page et al. 2021, and Section 3.1), V1674 Her was detected in the course of the SRG/eROSITA survey (Galiullin & Gilfanov 2021). Radio emission from V1674 Her was detected using the VLA (Sokolovsky et al. 2021; Sections 3.4 and 4.4). The very long baseline interferometry (VLBI) observation with e-EVN on t_0 + 10 d resulted in an upper limit (Paragi et al. 2021).

A remarkable feature of V1674 Her is the emergence of orbital (3.67 h = 0.153 d; Schmidt, Shugarov & Afonina 2021; Shugarov & Afonina 2021) and white dwarf spin periods (8.36 min = 0.00580 d; Patterson et al. 2021) shortly after the eruption. The two periods are seen in X-rays in addition to optical data (Maccarone et al. 2021; Pei et al. 2021; Lin et al. 2022; Page et al. 2022; Orio et al. 2022a). The spin period was present before the eruption according to the Zwicky Transient Facility photometry reported by Mroz et al. (2021). The spin period change may be caused by some combination of magnetic coupling between the rotating white dwarf and the ejecta, non-rigid rotation or substantial radial expansion of the heated white dwarf. Following the spin-down associated with the eruption, a spin-up in the post-eruption phase is reported by Patterson et al. (2022) on the basis of optical photometry, while the presence of changes in the X-ray derived period deserves further investigation (Drake et al. 2021; Orio et al. 2022a).

The 3.67 h orbital period firmly identifies the donor star as a dwarf: an evolved donor would not fit in such a compact orbit (Knigge, Baraffe & Patterson 2011). The white dwarf spin period is substantially shorter than the orbital period, revealing the system as an intermediate polar (IP). IPs host white dwarfs with magnetic fields strong enough to disrupt the inner part of the accretion disc and redirect the accreting matter to the magnetic poles. As the white dwarf rotates, the magnetic poles come in and out of view modulating the X-ray and optical light of the system (see the reviews by Patterson 1994, Buckley 2000, Mukai 2017).

Astrometric measurements during the eruption of V1674 Her (e.g. Aydi et al. 2021) allow the identification of the nova progenitor as a $G = 19.95 \pm 0.02$ star *Gaia* DR3 4514092717838547584 located at RA and Dec.

`18:57:30.98324 + 16:53:39.5895`equinox J2000.0, mean epoch 2016.0; with the positional uncertainty of 0.6 and 0.8 mas and the proper motion of -4.1 ± 0.7 and -4.7 ± 0.9 mas yr^{-1} in RA and Dec. directions, respectively; there is no measured parallax (Gaia Collaboration 2016, 2022). The detection of the white dwarf spin period in the pre-eruption Zwicky Transient Facility (Masci et al. 2019) photometry by Mroz et al. (2021) unambiguously confirms the progenitor identification.

Munari et al. (2021) report $E(B - V) = 0.55$ mag based on the Munari & Zwitter (1997) relation between extinction and the equivalent width of the K I 7699 Å line. For the standard value of

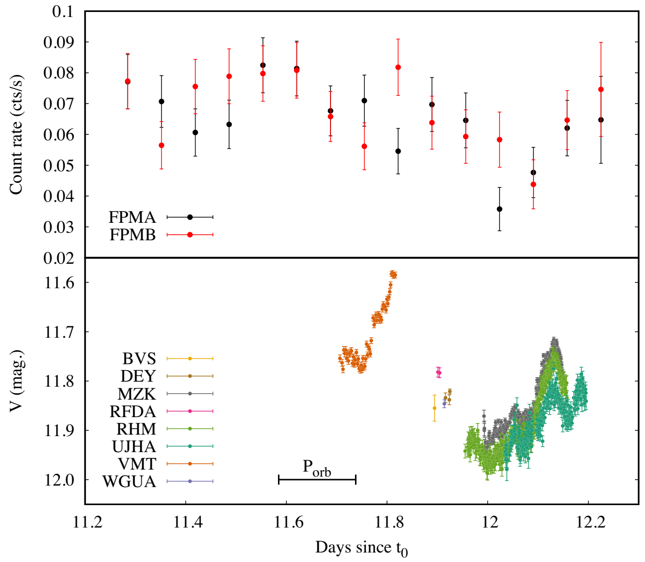

Figure 2. Top panel: the background-subtracted 3.0–30 keV *NuSTAR* light curve of V1674 Her (see Section 3.1.1). Bottom panel: simultaneous optical *V* band photometry by multiple observers identified by their AAVSO codes. The horizontal bar indicates the duration of V1674 Her orbital period.

$\frac{A_V}{E(B-V)} = 3.1$, this corresponds to $A_V = 1.70$ mag. We use A_V to estimate the expected Galactic X-ray absorbing column to V1674 Her following Güver & Özel (2009):

$$N_{\rm H} = 2.21 \times 10^{21}\,{\rm cm}^{-2} \times A_V = 3.77 \times 10^{21}\,{\rm cm}^{-2} \qquad (1)$$

– this is the value we use throughout this paper. The total line of sight neutral hydrogen column density in this direction, as derived from the 21-cm line observations of Kalberla et al. (2005), is $N_{\rm H\,I} = 2.99 \times 10^{21}$ cm^{-2}, lower than the above optical reddening-based estimate. The similar value $N_{\rm H\,I} = 2.95 \times 10^{21}$ cm^{-2} is listed in the H I 4π survey data (HI4PI; HI4PI Collaboration 2016).

3 OBSERVATIONS AND ANALYSIS

3.1 *NuSTAR* hard X-ray observations

NuSTAR is a focusing hard X-ray telescope operating in the 3–79 keV energy range (Harrison et al. 2013; Madsen et al. 2015). *NuSTAR* observed V1674 Her between 2021-06-23 11:24 (t_0 + 11.3 d) and 2021-06-24 10:24 UT (ObsID 90701321002; PI: Sokolovsky) for a total exposure of 39 ks. For the analysis, we used NUPIPELINE and NUPRODUCTS scripts from HEASOFT V6.30.1 (HEASARC 2014), together with the calibration files from the CALDB version 20220706. Following the same analysis procedure as Sokolovsky et al. (2020, 2022a), we utilized a circular extraction region with radius of 30 arcsec centred on the X-ray image of the nova using DS9 (Joye & Mandel 2003) independently for the two focal plane modules: FPMA and FPMB. The background was extracted from five circular regions of the same radius placed on the same Cadmium-Zinc-Telluride (CZT; Arnaud, Smith & Siemiginowska 2011) chip as the nova image. For the following analysis we restricted the energy range to 3.0–30 keV.

3.1.1 NuSTAR *light curve*

Fig. 2 presents the 3.0–30 keV light curves of V1674 Her obtained during the *NuSTAR* observation described in Section 3.1.2. The light curves were background-subtracted and binned to 5804 s (corresponding to the *NuSTAR* orbital period at the time of the observations) resulting in one count rate measurement per orbit. Following de Diego (2010) and Sokolovsky et al. (2017), we perform a χ^2 test to evaluate the significance of the count rate variations. The probability of the observed scatter of count rate measurements arising from random noise (while the true count rate is constant) is found to be very low (0.0003), allowing us to reject the constant count rate hypothesis. The detected variations are happening on time-scales from one *NuSTAR* orbit to the total duration of the observation. The mean background-subtracted count rate is 0.065 ct s^{-1} per focal plane module.

We searched for periodicities in photon arrival times using the PATPC[2] code (Sokolovsky et al. 2022b) constructing the 'H_m-periodogram' (de Jager, Raubenheimer & Swanepoel 1989; de Jager & Büsching 2010; Kerr 2011). No periodicities were identified in the trial period range of 1 to 1000 s that would satisfy the following criteria:

(i) be significant at $p < 0.05$ level (Section 1);
(ii) be present in both FPMA and FPMB data;
(iii) not be a multiple of the *NuSTAR* orbital period.

We repeated the search restricting the analysis to the lowest-energy 3.0–3.5 keV events with the same null result. Finally, we compute the H_m value for the spin and orbital periods reported by Patterson et al. (2022) and find the associated single-trial probabilities to be $p \gg 0.05$ (no significant periodicity in *NuSTAR* data).

We note that irregular variability is present in the AAVSO optical photometry obtained simultaneously with the *NuSTAR* observations (Fig. 2). This variability is distinct from the overall optical brightness decline and is happening on a time-scale longer than the orbital period. The spin variations were first detected after the *NuSTAR* epoch (Patterson et al. 2022). The physical origin of these irregular brightness variations is uncertain.

3.1.2 NuSTAR *spectroscopy*

The *NuSTAR* FPMA and FPMB spectra (Fig. 3) were binned to have at least 25 counts per bin and were fit jointly using the models listed in Table 1. All the considered models include a `constant` component to account for the imperfect (and variable) cross-calibration of FPMA and FPMB, a `phabs` component that accounts for the photoelectric absorption (Balucinska-Church & McCammon 1992) in the Galaxy along the line of sight by solar abundance material (Asplund et al. 2009; the equivalent hydrogen column density, $N_{\rm H}$, is fixed to the value listed in Section 2); and a `vphabs` component that accounts for the possible intrinsic absorption within the nova shell ($N_{\rm H}$ and the abundances associated with this model component are varied).

The simplest X-ray emission model we consider is `powerlaw`. Allowing both the photon index and the intrinsic photoelectric absorption to vary, one can account for the observed curvature of the spectrum and obtain a good fit even with the solar abundance absorber, see Table 1 and Fig. 3. However, as discussed by Sokolovsky et al. (2022a), the non-thermal X-ray emission mechanisms expected to operate in a nova should all produce hard photon spectra. Vurm & Metzger (2018) predict that the low-energy extension of the GeV emission should have a Γ = 1.2 to 1.0 in the *NuSTAR* band. The other possible non-thermal mechanism – Comptonization of the radioactive MeV lines – should produce even harder spectra with

---

[2] https://github.com/kirxkirx/patpc

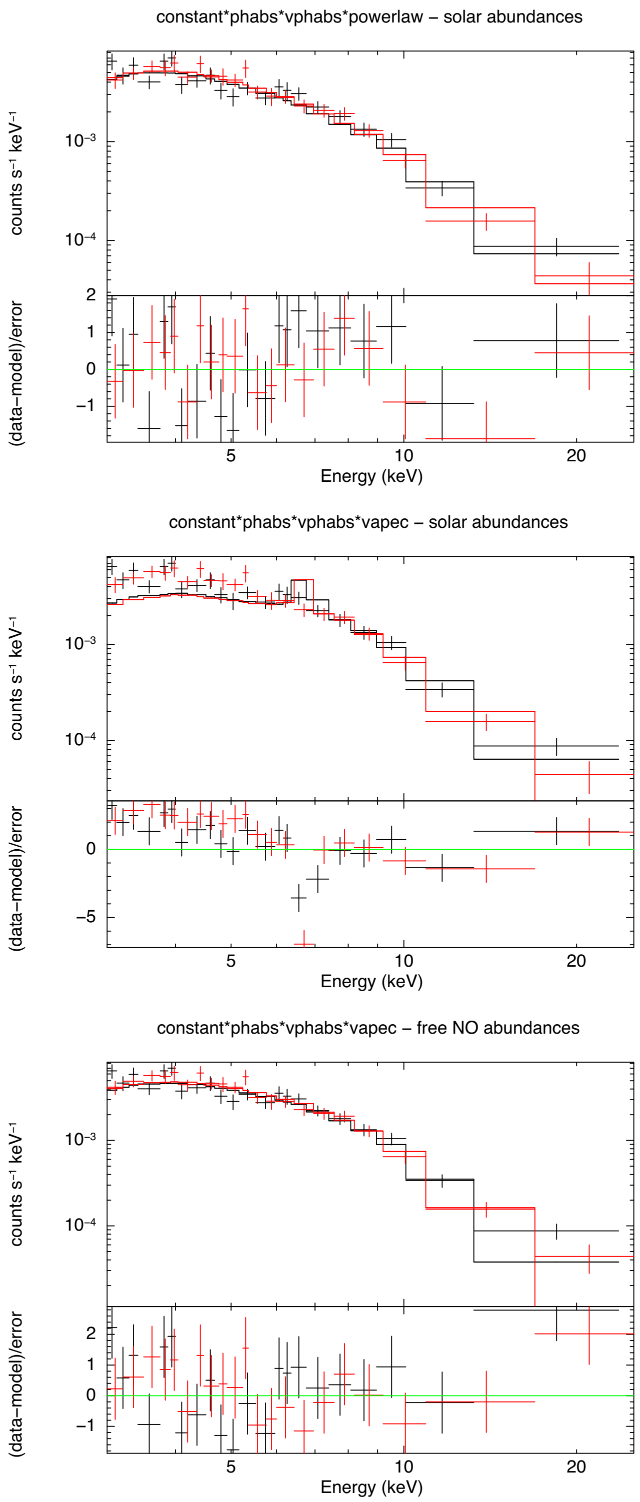
constant*phabs*vphabs*powerlaw – solar abundances

constant*phabs*vphabs*vapec – solar abundances

constant*phabs*vphabs*vapec – free NO abundances

Figure 3. Observed *NuSTAR* spectra compared with the models from Table 1: power-law emission with solar abundance absorber (top), APEC thermal plasma emission with solar abundances for both the emitter and absorber (middle), and the APEC model, with NO abundances tied together and left free to vary (bottom). Black and red represent spectra obtained with the two *NuSTAR* telescopes: FPMA and FPMB. For each model, the top sub-panel shows the spectrum and the model, while the bottom sub-panel shows the difference between the spectrum and the model in the units of uncertainty associated with each data bin.

$\Gamma \lesssim 0$ below 30 keV (see figs 1–4 of Gomez-Gomar et al. 1998). The observed soft photon index $\Gamma = 3.2 \pm 0.1$ contradicts these predictions.

The power law provides a convenient empirical description of the data, so we use it to compute the monochromatic flux (in SED units; Section 1) at 20 keV (where the absorption is negligible, simplifying the computations) using equation (4) of Sokolovsky et al. (2022a): $\nu F_\nu = 3.6 \times 10^{-10}\,\mathrm{erg\,cm^{-2}\,s^{-1}}$. In the absence of an obvious physical mechanism that would produce non-thermal emission with a soft power-law spectrum, we favour thermal emission models.

The GeV (Section 3.3) and non-thermal radio (Section 4.4) emission reveal the presence of shock-accelerated particles within the ejecta of V1674 Her. Shocks may heat plasma to X-ray temperatures (e.g. Zel'dovich & Raizer 1967; Dyson & Williams 1997). Thermal emission of shock-heated plasma is the standard explanation for the $\gtrsim 1$ keV X-rays observed from novae (Section 1). Therefore, we attempt a fit with a collisionally ionized plasma emission model (`vapec`; Brickhouse et al. 2005). The model includes both the bremsstrahlung (free–free) continuum and line emission from specific elements.

We found no acceptable fit (Section 1) to the data with the elemental abundances of the emitting plasma and the absorber fixed to the solar values (Table 1). Specifically, the `apec` model predicts a strong Fe Kα emission feature at 6.7 keV that is clearly not present in the data (Fig. 3). While fitting the solar-abundance `apec` model, XSPEC is trying to suppress the Fe Kα emission by increasing the temperature (compared to the non-solar abundances fits), essentially trading off the reduced residuals in the 6–7 keV region for the increased residuals in the low energy regions.

One may change the elemental abundances in the `vapec` model to suppress the Fe Kα emission relative to the bremsstrahlung continuum. There are two ways to do this:

(i) decrease the Fe abundance to suppress the emission;
(ii) increase abundances of other heavy elements that, being ionized, will shed more free electrons, enhancing the bremsstrahlung continuum (and swamping the Fe emission).

Nova ejecta are known to be overabundant in CNO elements (Williams 1985; Truran & Livio 1986; Gehrz et al. 1998; Schwarz et al. 2001; Vanlandingham et al. 2005; Helton et al. 2012). The obvious explanation for such overabundance is that nova ejecta contain material ablated from the white dwarf with CO or ONeMg composition (e.g. Shara et al. 2018; Das 2021, and references therein). Nitrogen is usually the most abundant of the CNO elements as the accreted material is mixed with the white dwarf material and processed through the incomplete CNO cycle (Starrfield et al. 1972; Truran & Livio 1986) that changes the relative abundance of the CNO elements. The cycle is most likely to be interrupted by ejection while in the ^{14}N bottleneck (e.g. Imbriani et al. 2004; LUNA Collaboration 2006). The exact composition of the ejecta depends on the degree of mixing between the accreted envelope and the white dwarf (Casanova et al. 2011, 2016; Denissenkov et al. 2013; Casanova, José & Shore 2018; Guo, Wu & Wang 2022) as well as the white dwarf composition. To account for this, we let the abundances of the emitting plasma and the absorber intrinsic to the nova ejecta vary. We also consider abundances for the emitter and absorber fixed to those found in another nova where they are well constrained, and consider solar abundance for comparison. We assume that the emitting and absorbing material both originate in the nova ejecta and have the same elemental abundances. The Galactic absorber along the line of sight is assumed to have solar abundances and is represented by a separate model component `phabs`, as described earlier.

Table 1. *NuSTAR* spectral modelling.

`vphabs` $N_{\rm H}$ (10^{22} cm^{-2})	kT (keV)	Γ	C/C$_\odot$, N/N$_\odot$, O/O$_\odot$, Ne/Ne$_\odot$, Mg/Mg$_\odot$, Si/Si$_\odot$, S/S$_\odot$, Fe/Fe$_\odot$	3.0–30 keV Flux $\log_{10}$(erg cm^{-2} s^{-1})	unabs. 3.0–30 keV Flux $\log_{10}$(erg cm^{-2} s^{-1})	p	χ^2/d.o.f.
solar abundances `constant*phabs*vphabs*powerlaw`							
5.0 ± 2.1		3.2 ± 0.1	$1.0*, 1.0*, 1.0*, 1.0*, 1.0*, 1.0*, 1.0*, 1.0*$	-11.65 ± 0.01	-11.59 ± 0.03	0.50	62.24/63
solar abundances `constant*phabs*vphabs*vapec`							
$0.0^\dagger$	5.9 ± 0.3		$1.0*, 1.0*, 1.0*, 1.0*, 1.0*, 1.0*, 1.0*, 1.0*$	-11.72 ± 0.01	-11.72 ± 0.01	0.00	219.60/63
free NO abundances `constant*phabs*vphabs*vapec`							
$0.0^\dagger$	3.9 ± 0.2		$1.0*, 1000.0^\dagger, 1000.0*, 1.0*, 1.0*, 1.0*, 1.0*, 1.0*$	-11.69 ± 0.01	-11.71 ± 0.01	0.30	67.33/62
preferred model – V906 Car abundances `constant*phabs*vphabs*vapec`							
$0.0^\dagger$	4.1 ± 0.2		$1.0*, 345.0*, 29.0*, 2.2*, 0.6*, 1.1*, 1.0*, 0.1*$	-11.69 ± 0.01	-11.70 ± 0.01	0.39	65.52/63
V838 Her abundances `constant*phabs*vphabs*vapec`							
$0.0^\dagger$	3.5 ± 0.2		$7.5*, 37.9*, 1.9*, 52.5*, 1.4*, 7.2*, 32.8*, 1.5*$	-11.71 ± 0.01	-11.72 ± 0.01	0.00	131.52/63

Note. The parameters that were kept fixed for the model fit are marked with the $*$ symbol. The † symbol marks the limit of the search range reached during the fitting procedure: the best-fitting value is set equal to the limit value and no fitting uncertainty is reported. **Column designation:** Col. 1 – intrinsic absorbing column (in excess of the total Galactic value); Col. 2 – temperature of the thermal component; Col. 3 – photon index of the power law component; Col. 4 – abundances of selected elements by number relative to the solar values of Asplund et al. (2009); Col. 5 – the logarithm of the integrated 3.0–30 keV flux under the model; Col. 6 – logarithm of the unabsorbed 3.0–30 keV flux; Col. 7 – chance occurrence (null hypothesis) probability; Col. 8 – χ^2 value divided by the number of degrees of freedom.

All the emission features of elements C, N, O, Ne, Mg, Si, or S, as well as their absorption K edges, are outside the *NuSTAR* band. Therefore, the *NuSTAR* spectrum allows us to constrain only the total number of these medium-Z elements, not the individual abundances. To facilitate direct comparison with the results of Sokolovsky et al. (2020, 2022a), we tie together the abundances of N and O and let them vary while keeping the abundances of all other elements (including C and Fe) fixed to the solar values. While the abundances of N and O are clearly super-solar, the exact values are not well constrained (Table 1). Good fits can be obtained even if we allow the abundance of any one of the C, N, O, Si elements vary while keeping all other abundances fixed to solar. This illustrates that the individual contributions of these elements cannot be really distinguished based on our *NuSTAR* spectrum and only their overall contribution is constrained.

To pick some specific illustrative values, we consider a model with the abundances of N, O (along with Ne, Mg, and Si, and in addition tied-together Fe, Co, and Ni) fixed to the ones derived from *XMM–Newton* grating spectroscopy of a brighter nova V906 Car (Sokolovsky et al. 2020). The absorbed thermal plasma model with the V906 Car abundances provides an excellent fit to the *NuSTAR* spectrum of V1674 Her (Table 1; Fig. 4).

Wagner et al. (2021) classify V1674 Her as a neon nova based on strong forbidden Ne emission revealed by their optical spectroscopy. As nova V906 Car erupted on a CO white dwarf (Sokolovsky et al. 2020), we also tried to fit the *NuSTAR* spectra with the abundances of V838 Her – a fast neon nova with well-determined elemental composition (Schwarz et al. 2007). This model, however, did not result in a good fit: it overpredicted the Fe Kα 6.7 keV emission – the same problem that led us to reject the solar abundances fit.

In all variations of the absorbed thermal emission model, the intrinsic absorbing column is consistent with zero. The Galactic absorption is sufficient to describe the curvature of the *NuSTAR* spectrum.

3.2 *Swift* X-ray and UV observations

The Neil Gehrels Swift Observatory (Gehrels et al. 2004) combines multiple instruments including the X-ray Telescope (XRT; Burrows et al. 2005) operating in the 0.3–10 keV energy range and the UV/Optical Telescope (UVOT; Roming et al. 2005) on a space-based platform capable of fast repointing. A detailed discussion of the *Swift*/XRT light curve of V1674 Her is presented by Drake et al. (2021). Here, we analyse the *Swift* observation performed on 2021-06-24 (ObsID 00014375014; PI Orio). The nova was observed for a total exposure of 1 ks split between two pointings around 02:49–02:53 and 12:25–12:37 UT, the first one overlapping with the *NuSTAR* observation described in Section 3.1. In order to minimize the optical loading we limited the analysis to `grade 0` events. V1674 Her is clearly detected in the 0.5–10.0 keV band by *Swift*/XRT at 0.091 ± 0.012 ct s^{-1}. The XRT spectrum presented in Fig. 4 is consistent with the same absorbed single-temperature model describing the *NuSTAR* observations, if we allow for a constant offset between the XRT and *NuSTAR* data. The `constant` $= 1.5 \pm 0.3$ offset accounts for the source variability (cf. Fig. 2) and the XRT to *NuSTAR* cross-calibration uncertainty (expected to be below 10 per cent; Madsen et al. 2017). We also used PATPC (Section 3.1.1) to test for the presence of X-ray modulation at the *spin* period in *Swift*/XRT events. The resulting single-trial H_m value corresponds to a chance occurrence probability of $p = 0.09$, which we consider a non-detection (Section 1). An individual *Swift* pointing is shorter than the *orbital* period. Investigations of X-ray orbital periodicity based on multiple *Swift* and *NICER* pointings are presented by Drake et al. (2021), Orio et al. (2022a), and Lin et al. (2022).

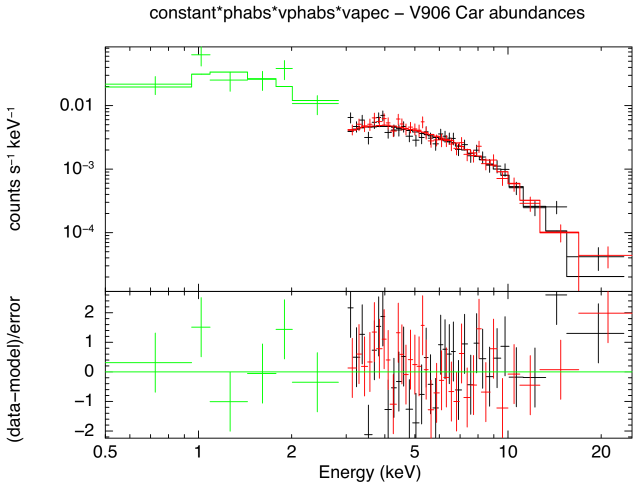

Figure 4. The quasi-simultaneous *NuSTAR*/FPMA and FPMB (colour coded as black and red, respectively) and *Swift*/XRT (green) spectra of V1674 Her compared to our preferred model – the single-temperature absorbed thermal plasma with the elemental abundances set to match those of nova V906 Car (Sokolovsky et al. 2020).

The simultaneous ultraviolet photometry with *Swift*/UVOT resulted in the Vega system magnitudes uvw2 = 12.10 ± 0.02, uvm2 = 12.87 ± 0.03, uvw1 = 11.59 ± 0.02, corresponding to a blackbody temperature of $T_{\rm UVOT} = 27\,000 \pm 4000$ K. To compute $T_{\rm UVOT}$ we applied the reddening correction (Section 2) using Cardelli, Clayton & Mathis (1989) extinction law and the UVOT magnitude-to-flux conversion of Poole et al. (2008).

3.3 *Fermi*-LAT γ-ray observations

The *Fermi*-LAT (Atwood et al. 2009) is a γ-ray instrument sensitive to the 30 MeV–2 TeV energy range. We used FERMITOOLS version 2.0.8[3] (Fermi Science Support Development Team 2019) to perform a binned Maximum Likelihood analysis (Mattox et al. 1996) of *Fermi*-LAT data on V1674 Her. We selected Pass 8 data (`P8R3`; Atwood et al. 2013; Bruel et al. 2018; with the associated `P8R3_V3` instrument response functions) `SOURCE` class events, in the energy range 0.1–300 GeV, with maximum zenith angle of 90°, and with reconstructed positions within 15° of (RA, Dec.) = (285°.0, 16°.5). The centre of the region of interest (ROI) was offset slightly (0°.71) from the optical position of V1674 Her in order not to place the nova at the corner of spatial four bins (the bins were 0.1° on a side). The events were filtered to include only times when the observatory was in normal science operations and the data were flagged as good. The events were spatially binned in a 21°.2 × 21°.2 square region (sized to fit within the 15° radius circular selection) and were binned in log (energy) in 35 bins of equal size. Energy dispersion (finite energy resolution of LAT) correction was enabled for all of our likelihood analyses, though the correction was disabled for the isotropic diffuse emission component.[4]

We constructed a spatial and spectral model of the region by including all point and extended sources from the third data release of the *Fermi* LAT fourth source catalogue (4FGL-DR3; Abdollahi et al. 2020) within 25° of the ROI centre. The model includes sources that are outside the field of view defined by the photon arrival direction selection at the previous step. We checked that the spectral analysis results do not depend critically on the exact choice of the model source and photon selection radii. The model also included components for the Galactic (using the spectral-spatial template `gll_iem_v07.fits`) and isotropic (using the file function `iso_P8R3_SOURCE_V3_v1.txt`) diffuse emission.[5] For our initial analysis, the spectral parameters of point sources detected in 4FGL-DR3 with ≥15σ average significance and within 6° of the ROI centre were allowed to vary in the fit, as well as the normalizations of the diffuse components. Additionally, the normalization parameters of sources flagged as variable in 4FGL-DR3 were allowed to vary if they were within 8° of the ROI centre. A point source was added at the optical position of V1674 Her having the `PowerLaw2` spectral model,[6] with the `Integral` parameter free to vary, the photon index (Γ) fixed to a value of 2.2 (typical for γ-ray novae; Section 4.1), the lower-limit (upper-limit) parameter fixed at 0.1 GeV (300 GeV).

To refine the free parameters in our model, we analysed one year of data prior to the outburst (2020-06-01 to 2021-06-01). After an initial fit, examination of the spatial residuals suggested that the normalization of the point source 4FGL J1930.3+0911 needed to be free to vary. Additionally, the point source at the position of V1674 Her was not significantly detected and was removed from the model before refitting.

We then analysed data spanning 40 days from $t_0 - 10$ d to $t_0 + 30$ d. We started from the model best-fitting the one-year pre-eruption data, as described above. We added a point source at the optical position of V1674 Her, fixed the spectral parameters of the Galactic diffuse emission, and fixed all but the normalization parameters for sources that were free to vary in the previous analysis. Finally, we fixed the normalizations of the faint sources that were detected with the test statistic TS < 9 (Mattox et al. 1996) in the 40-d data to their respective 1-yr values. The new source at the nova position was detected with TS = 5 during this 40-d time interval, which is just less than 2σ for two degrees of freedom.

Using the 40-d model as a starting point, we constructed a light curve with 6 h bins (Fig. 1) spanning $t_0 \pm 2$ d. We assumed a power-law spectrum for the nova with free normalization and photon index. The nova was detected in three consecutive 6 h bins, with the first detection at $t_0 + 6$ h having TS = 31. We consider as detections the 6 h bins with TS > = 6 (2σ detection for two degrees of freedom) and at least 4 predicted counts, while calculating the 95 per cent upper limits for the other bins (Fig. 1). According to Lin et al. (2022), this is the shortest-duration γ-ray nova ever observed.

During the 18 h time span covered by the detections, V1674 Her was identified with TS = 49 (Fig. 5), having $\Gamma = 2.3 \pm 0.2$. The 0.1–300 GeV photon flux is $(1.6 \pm 0.4) \times 10^{-6}$ photons cm^{-2} s^{-1}, which is equivalent to an integrated energy flux of $(9.5 \pm 2.7) \times 10^{-10}$ erg cm^{-2} s^{-1}. Using `gtfindsrc` on this 18-h interval, we found a best-fitting position for the γ-ray point source of (RA, Dec.) = (284°.17, 16°.86), offset from the nova optical position by 0°.20, well within the 95 per cent confidence-level containment radius of 0°.26. Starting with the full-energy range 18-h model, we constructed the SED of V1674 Her by performing fitting in individual energy bands. The monochromatic flux values in Fig. 6 are shown for the bins where the nova was detected with TS ≥ 4 and had at least four predicted counts, otherwise a 95 per cent confidence-level upper limit is reported.

No significant improvement (maximum ΔTS = 3) was found by changing the source spectrum model to a curved log-parabola or power law with an exponential cut-off or hadronic model. For the hadronic model the integrated 0.1–300 GeV flux is $(1.4 \pm 0.3) \times 10^{-6}$ photons cm^{-2} s^{-1} for a best fitting slope of the power-law proton spectrum $3.0^{+0.6}_{-0.3}$. The hadronic model uses the method of Kamae et al. (2006) to calculate the γ-ray spectrum due to the decay of neutral pions produced in proton-proton collisions. This model was applied to novae earlier by Abdo et al. (2010), Ackermann et al. (2014), and Cheung et al. (2022).

While we cannot prefer an exponential cut-off over a simple power law on the basis of the available photon data, we still perform the exponential cut-off fit to facilitate comparison with previously detected LAT novae. For V1674 Her the exponential cut-off is found at 0.4 ± 0.3 GeV, and the photon index $\Gamma = 0.9 \pm 0.9$ is harder than what is predicted by the simple power-law model. For the exponential cut-off power-law model, the integrated 0.1–300 GeV photon flux is $(1.3 \pm 0.4) \times 10^{-6}$ photons cm^{-2} s^{-1} equivalent to an integrated energy flux of $(6.7 \pm 1.5) \times 10^{-10}$ erg cm^{-2} s^{-1}. The corresponding monochromatic flux (SED point; Section 1) at 100 MeV is $\nu F_\nu = 1.5 \times 10^{-10}$ erg cm^{-2} s^{-1} where we used equation (3) of Sokolovsky et al. (2022a) to convert the FERMITOOLS model parameters to νF_ν.

---

[3] https://github.com/fermi-lat/Fermitools-conda/

[4] https://fermi.gsfc.nasa.gov/ssc/data/analysis/documentation/Pass8_edisp_usage.html

[5] Both files are available for download at https://fermi.gsfc.nasa.gov/ssc/data/access/lat/BackgroundModels.html

[6] https://fermi.gsfc.nasa.gov/ssc/data/analysis/scitools/source_models.html#PowerLaw2

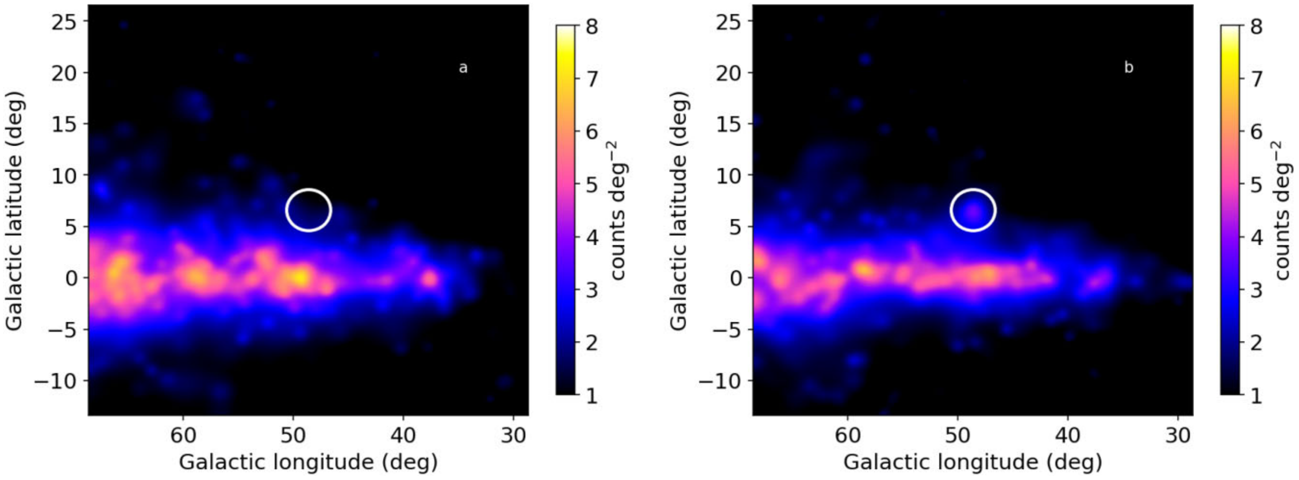

Figure 5. The *Fermi*-LAT smoothed 0.1–2 GeV count images centered on V1674 Her. The left image (a) covers the time interval 2021-06-10 10:34 to 2021-06-11 08:34 UT before the eruption. The right image (b) covers the 18 h interval when the γ-ray emission was detected. The white circle marks the optical position of the nova.

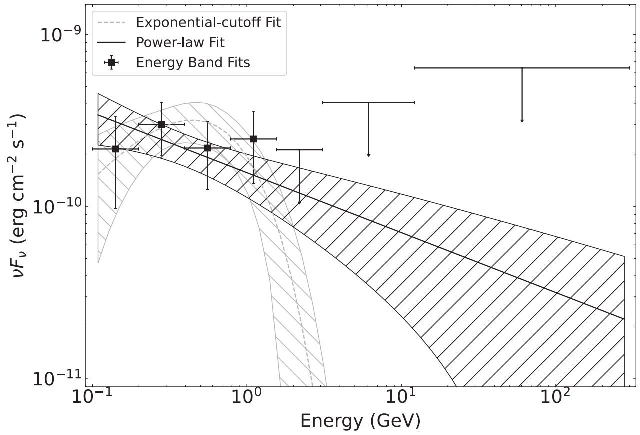

Figure 6. The *Fermi*-LAT spectral energy distribution of V1674 Her, compared to the power law (solid black line) and power law with an exponential cut-off (dashed grey line) models. The models were fit to the 0.1–300 GeV photon data using the maximum likelihood technique. The filled regions correspond to the 1σ uncertainty range for the power law (black, forward slash fill) and cutoff (grey, back slash fill) models.

For comparison with previous γ-ray novae, we computed the average γ-ray to optical luminosity ratio of V1674 Her between day $t_0 + 6$ h and day $t_0 + 24$ h. The optical flux changes by a factor of two over that 18 h time interval passing its peak. To estimate average optical flux over the time interval of the detected γ-ray emission we fitted a fireball model to the Evryscope (g band), MLO-ASC and AAVSO (V-band and visual magnitudes) data assuming a blackbody temperature of 8000 K. The fireball model calculates the light curve emitted by an expanding ionized ejecta (e.g. see section 5 of Munari, Hambsch & Frigo 2017, and references therein). The resulting γ-ray to optical luminosity ratio ranges from $(2.1 \pm 0.4) \times 10^{-3}$ to $(2.7 \pm 0.5) \times 10^{-3}$ for a γ-ray spectral distribution described by an exponential cut-off power-law and a hadronic model, respectively. These ratios are similar to the ones obtained with other γ-ray novae (Metzger et al. 2015; Li et al. 2017; Aydi et al. 2020a; Cheung et al. 2022).

The analysis of *Fermi*-LAT data over the time interval matching the *NuSTAR* observation (Section 3.1) results in non-detection with a 95 per cent upper limit on the photon flux of $<4 \times 10^{-7}$ photons cm^{-2} s^{-1} (0.1–300 GeV integrated energy flux less than 2.2×10^{-10} erg cm^{-2} s^{-1}.).

Finally, we tested for the presence of orbital and spin periodicities (Patterson et al. 2022) in the γ-ray photon arrival times. For the test we selected 19 events within 5° of V1674 Her (recorded during the time it has been detected by *Fermi*-LAT) and assigned to the nova with a GTSRCPROB probability of at least 68 per cent. The event times were corrected to the Solar system barycentre with GTBARY. We used PATPC (Section 3.1.1) to compute the H_m values for the orbital and spin periods and the corresponding probability of obtaining this H_m value by chance. The events were found to be consistent with arriving at random phases for both trial periods (no periodicity found). This is in line with the results of Lin et al. (2022) who report no significant periodicity in the γ-ray data.

3.4 VLA radio observations

The National Radio Astronomy Observatory's Karl G. Jansky Very Large Array consists of 27, 25 m-diameter radio telescopes combined to form a connected interferometer operating in a 0.07–50 GHz frequency range (Thompson et al. 1980; Perley et al. 2011), see Thompson, Moran & Swenson (2017) for a detailed discussion of radio interferometry techniques. We observed V1674 Her with the VLA at 15 epochs between 2021-06-15 ($t_0 + 3.2$ d) and 2022-07-26 ($t_0 + 409.1$ d). Most observations were performed while the array was in its C configuration (baseline range 0.035–3.4 km). At each epoch a 1 h 45 min observation was split between S, C, K_u, and K_a bands. The data at each band were further split in two adjacent sub-bands to improve spectral resolution. The images were reconstructed independently at the following central frequencies: 2.6, 3.4, 5.1, 7.0, 13.7, 16.5, 31.1, 34.9 GHz. The VLA observing log is presented in Table 2.

We used the quasar J1857+1624 (GB6 B1855+1620; located 0°.48 from V1674 Her) as the complex gain calibrator. 3C 48 was used to set the absolute flux density scale with the exception of the observations on 2021-06-25 and 2021-07-13 when 3C 286 was used (Table 2; Perley & Butler 2017; c.f. Taylor et al. 1987). For each observing epoch we produced two versions of the VLA schedule optimized for different local sidereal time ranges to facilitate dynamic scheduling. One version had 3C 48 scans at the end of the experiment while the other started with the scans on 3C 286. Following Chomiuk

Table 2. VLA observing log.

Epoch	Days since t_0	Date	ID	VLA config.	Prim. calib.
1	3.2	2021-06-15	SD1113	C	3C 48
2	4.2	2021-06-16	SD1113	C	3C 48
3	5.2	2021-06-17	SD1113	C	3C 48
4	9.2	2021-06-21	SD1113	C	3C 48
5	10.1	2021-06-22	SD1113	C	3C 48
6	13.1	2021-06-25	SD1113	C	3C 286
7	15.2	2021-06-27	SD1113	C	3C 48
8	31.0	2021-07-13	SD1113	C	3C 286
9	44.1	2021-07-26	SD1113	C	3C 48
10	74.0	2021-08-25	SD1113	C	3C 48
11	83.0	2021-09-03	SD1113	C	3C 48
12	91.0	2021-09-11	SD1113	C	3C 48
13	142.8	2021-11-01	21B-351	B	3C 48
14	315.4	2022-04-23	22A-169	A	3C 48
15	409.1	2022-07-26	22A-169	D	3C 48

et al. (2021b) we expect the absolute flux density uncertainty to be 5 per cent (10 per cent) at frequencies below (above) 10 GHz. As we rely on phase transfer from the phase calibrator and do not attempt self-calibration (as the target is rather weak), there might be an additional uncertainty as large as a few tens of per cent at high frequencies associated with imperfect phase transfer in bad weather.

We relied on the remotely accessible computing resources of the NRAO's New Mexico Array Science Center `nmpost` cluster for VLA data calibration and imaging. Specifically, we used CASA 6.1.2 (McMullin et al. 2007) with the VLA `pipeline 2020.1.0.40` for calibration, CASA 4.7.2 for writing out single sub-band multi-source `FITS` files that were loaded to AIPS 31DEC21 (Greisen 2003) for indexing and splitting into single-source `FITS` files suitable for imaging in DIFMAP 2.5E (Shepherd, Pearson & Taylor 1994; Shepherd 1997).

The `CLEAN` (Högbom 1974) imaging was performed in DIFMAP, which was also used for manually flagging the data affected by RFI or poor system performance (e.g. a warm receiver at a specific antenna). To identify the bad data that survived automated flagging by the CASA pipeline, we used DIFMAP's `radplot` command to inspect the correlated flux densities in the Stokes *V*, *Q*, and *U* parameters as a function of baseline length. These plots allow one to easily identify unusually noisy or highly polarized data points commonly associated with corrupted data. We then plot the Stokes I correlated flux density as a function of time for each pair of antennas (`vplot` with `vflags = '1f'`) and identify groups of flagged visibility measurements that affect the same frequency channels at multiple antennas (RFI) or multiple channels at one antenna (receiver problems) and flag all the visibilities in the affected groups of channels.

We tried two imaging strategies. First we `CLEAN`'ed the naturally weighted data by manually putting `CLEAN` windows around regions with visible emission, followed by a full-map `CLEAN` once no visible emission remains in the residual map. The second approach was to employ a version of Dan Homan's automated multi-resolution `CLEAN`'ing script[7] that `CLEAN`'s the full map first at super-uniform (`uvweight 10,-1`), then uniform (`uvweight 2,-1`) and natural weighting (`uvweight 0,-2`). The script does not rely on manually placed `CLEAN` windows and performs no self-calibration. The rationale behind the multiresolution `CLEAN`'ing was discussed by Moellenbrock (1999), and the script we utilize is the one used for analyzing Very Long Baseline Array data in the framework of the MOJAVE project (Lister et al. 2009). The results of the manual `CLEAN`'ing at the natural weighting and automated multi-scale `CLEAN`'ing were found to be very similar, with the multiscale procedure typically resulting in a slightly lower image noise, but on rare occasions, exaggerating a pattern of stripes crossing the image that result from amplitude calibration issues (for the datasets affected by this problem, manual `CLEAN`'ing reduced the amplitude of the stripes).

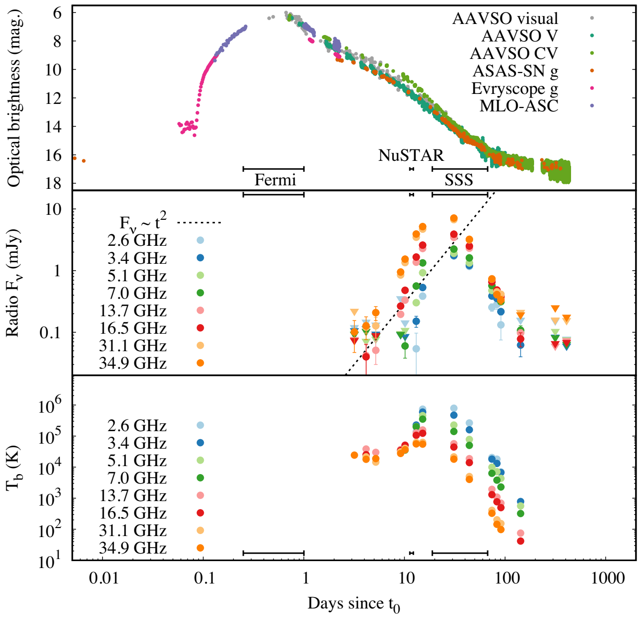

Figure 7. The optical (top panel) light curve of V1674 Her compared to the VLA radio light curve (middle panel) and the radio brightness temperature curve (bottom panel). The three horizontal bars indicate the time intervals when the γ-ray emission was detected by *Fermi*-LAT (left bar), the duration of the *NuSTAR* pointing (small bar in the middle) and the approximate duration of the SSS emission observed by *Swift*/XRT (right bar; from Drake et al. 2021). The dotted line indicates the rate at which a uniformly expanding optically thick thermal cloud would increase its flux density.

The image pixel size was chosen so that we have at least five pixels across the half-power beam width at the observing frequency. The nova flux density was measured simply by taking the image peak value near the nova position. We checked that the nova is consistent with being a point source even at 34.9 GHz by fitting variable-width Gaussian source model to the *uv*-data using DIFMAP. At frequencies/epochs where no emission at the nova position is visible we report an upper limit computed as (e.g. Nyamai et al. 2023)

$$\mathrm{UL} = \max(0,\ \mathrm{image\_value\_at\_nova\_position}) + 3 \times \mathrm{image\_rms}. \tag{2}$$

The first term accounts for the possible presence of sub-threshold flux from the source. The image is in the units of surface brightness (Jy per beam), so we assume the target source remains unresolved even when invisible to interpret the result as an upper limit on the total flux density.

The VLA light curve of V1674 Her is presented in Fig. 7 while the evolution of its radio spectrum is presented in Fig. 8. In the first observation at $t_0 + 3.2$ d, the radio emission at the optical position of the nova is barely detected at 34.9 GHz with a flux density of 0.10 ± 0.05 mJy. The next day ($t_0 + 4.2$ d) brings a secure detection of the nova at four high-frequency sub-bands revealing an inverted

---

[7] http://personal.denison.edu/~homand/final_clean_rms

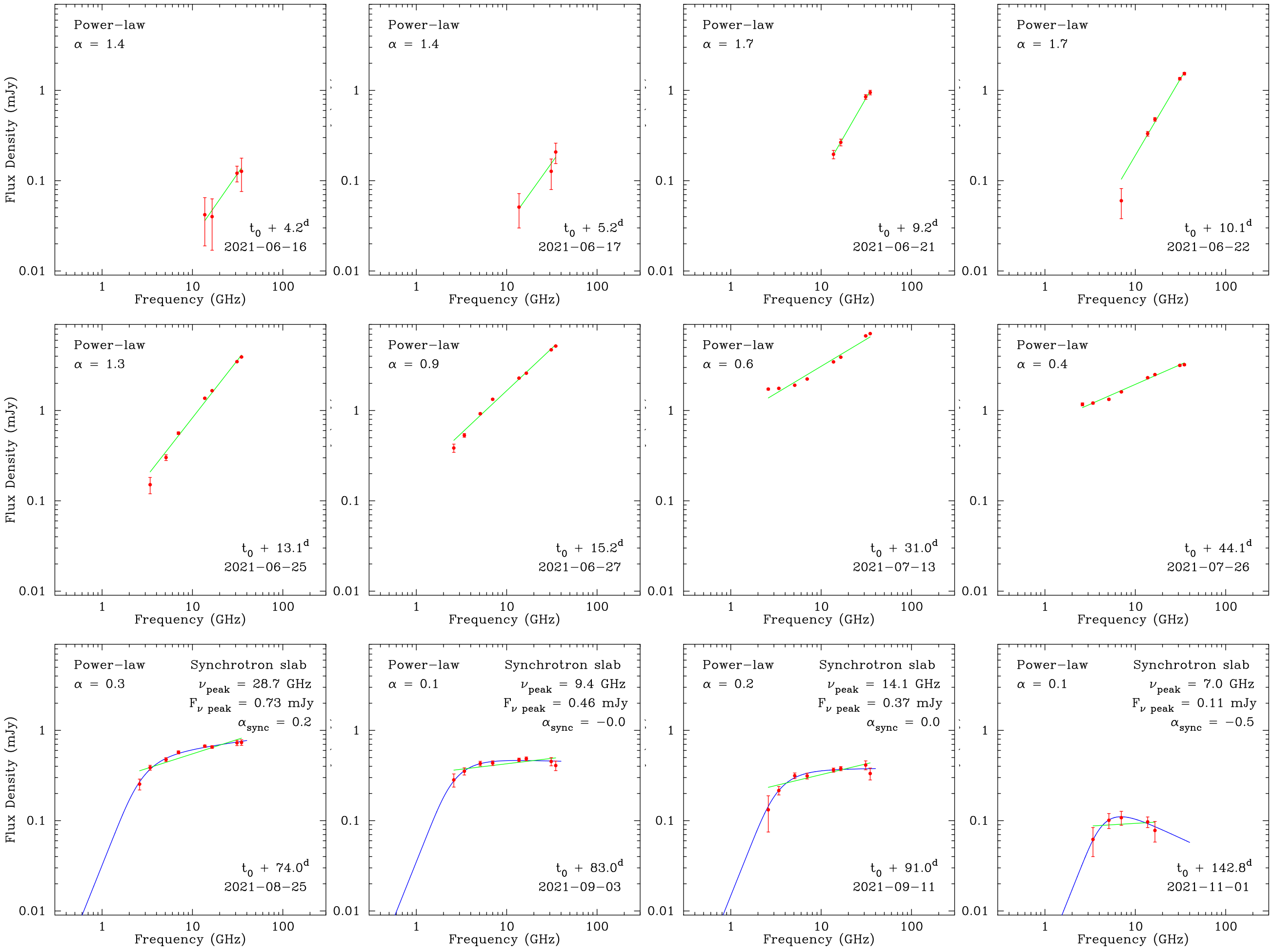

Figure 8. The evolution of the radio spectrum of V1674 Her. The VLA flux density measurements (red) are compared to the simple power-law fit (green line) and a spectrum of a uniform synchrotron-emitting slab (blue curve). The uncertainty on the spectral index is ∼0.3 for the power law fits on 2021-06-16, 2021-06-17, 2021-11-01 and $\lesssim 0.1$ in all other cases. The synchrotron slab spectrum can approximate the observations only at late epochs. The spectrum shape is most likely determined by the non-uniform optical depth across the source.

spectrum (Fig. 8). The flux densities continued increasing with time at all the observing frequencies, peaking around $t_0 + 31.0$ d at the values ranging from 1.73 ± 0.04 mJy at 2.6 GHz to 7.12 ± 0.04 mJy at 34.9 GHz (the quoted uncertainties reflect the residual map noise and do not include the systematic effects listed above). After the peak, the nova gradually fades, falling below the detection limit at all bands after $t_0 + 142.8$ d. The radio light curve appears rather smooth with a single peak characterized by a fast rise and slower decay. The peak and decline of the radio light curve coincide with the appearance of SSS X-ray emission (Fig. 7). As the eruption progresses, the radio spectrum gradually flattens out, becoming somewhat curved at the latest epochs (Fig. 8).

4 DISCUSSION

4.1 High-energy spectra

The featureless *NuSTAR* band emission, consistent with being produced by thermal plasma with non-solar abundances, is similar to that observed in classical novae previously detected by *NuSTAR*: YZ Ret (Sokolovsky et al. 2022a) and V906 Car (Sokolovsky et al. 2020). The *Swift*/XRT spectrum (obtained quasi-simultaneously with the *NuSTAR* pointing) is consistent with the thermal emission model attenuated by the Galactic absorption (Section 3.2). The first *NuSTAR*-detected classical nova V5855 Sgr (Nelson et al. 2019) also had a similar spectrum, but the photon statistics were too low to judge if the emitting plasma abundances were super-solar. *NuSTAR* observations of the other two classical novae, V339 Del and V5668 Sgr, resulted in non-detections (Vurm & Metzger 2018).

Two recurrent novae were also detected by *NuSTAR*: V745 Sco (Orio et al. 2015) and RS Oph (Luna et al. 2021, Orio, private communication). Unlike the classical novae, the spectra of both recurrent novae show strong Fe Kα emission. This can be understood as V745 Sco and RS Oph both being ‘embedded novae’ with red giant donors. Much of the shocked material in embedded novae originates in the giant’s wind that is likely to have nearly-solar composition (but see Delgado & Hernanz 2019 and Orio et al. 2022b). On the contrary, in classical novae we expect no dense circumbinary material (Hoard et al. 2014), so shocks must be internal to ejecta. The nova ejecta includes a lot of white dwarf material, making its elemental abundances highly non-solar.

The typical nova GeV photon index value differs between the simple power-law and exponential cut-off power-law models. Summarizing the spectral fits for the 14 classical novae (excluding the embedded nova V407 Cyg) reported by Cheung et al. (2016), Li et al. (2017, 2020), Franckowiak et al. (2018), Nelson et al. (2019), Gordon et al. (2021), Albert et al. (2022), and Sokolovsky et al. (2022a), for the simple power-law model the median photon index is $\Gamma = 2.20$ with a standard deviation of 0.14. Meanwhile for the exponential cut-off power-law, the median index is 1.84 with a standard deviation of 0.15 and the median cut-off energy is 3.0 GeV (standard deviation 1.6 GeV).

The slope of the *Fermi*-LAT spectrum of V1674 Her (Section 3.3; Fig. 6) is consistent with the typical Γ values cited above for the simple power-law model. Though we do not find significant evidence for spectral curvature, a cut-off energy below 1 GeV (if real) would be the smallest one to date among the *Fermi*-detected novae. The cut-off would reflect the particle energy spectrum, expected at a photon energy of 0.1 of the maximum particle energy according to Metzger et al. (2016). The shock velocity (estimated at a later epoch from the X-ray temperature, as described in Section 4.2), GeV luminosity (Section 4.3), and the low cut-off energy would place the V1674 Her shock in a region of surprisingly high density of $> 10^{11}$ cm^{-3} (see fig. 3 of Metzger et al. 2016). We stress that there is no evidence for the existence of a cut-off in the γ-ray spectrum of V1674 Her. The simple power law model provides an acceptable fit. We consider the model that includes the cut-off because it was preferred for other, brighter γ-ray novae.

In Section 4.6.3 we make a crude estimate of the density of the X-ray emitting plasma 11 d after eruption to be $\sim 10^6$ cm^{-3}. This estimate assumes that the X-ray plasma uniformly fills the whole volume of the ejecta. For a uniform expansion the volume should increase as the third power of time, so 10 days earlier, when the γ-ray emission was detected, the same plasma could have a factor of 1000 higher density. To reconcile the X-ray density estimate with the high density suggested by the low-energy cut-off in the γ-ray spectrum, we can assume that the X-ray emitting material should occupy less than 1 per cent of the ejecta volume. Considering that the X-ray emitting plasma may be confined in a thin shell that may cover only a fraction of a sphere, such an assumption does not seem impossible. Alternatively, rather than being an intrinsic feature of particle energy spectrum, the GeV cut-off may result from opacity (Section 4.7).

4.2 Shock location

Shocks in classical novae may result from parts of the nova shell being ejected at different times and at different speeds. There is evidence of multiple ejections in optical spectra of novae (Duerbeck 1987; Aydi et al. 2020b). The exact mechanism by which novae eject their envelope is debated (section 2.2 of Chomiuk et al. 2021a). As outlined in Section 1, it has been proposed both on observational (Chomiuk et al. 2014) and theoretical (Livio 1990; Shen & Quataert 2022) grounds that a nova eruption includes two phases of mass-loss driven by different mechanisms:

(i) The initial ejection of the common envelope formed by the expanded white dwarf atmosphere that engulfs the binary. The envelope is ejected by the binary motion and is concentrated towards the orbital plane of the binary (MacDonald 1980; Livio et al. 1990; Lloyd, O'Brien & Bode 1997).

(ii) The fast radiation-driven wind from the hot nuclear-burning white dwarf (Kato & Hachisu 1994; Friedjung 2011).

A similar interacting wind model was proposed to explain the shapes of planetary nebulae (Kwok 1982, Soker & Livio 1989, but see Balick & Frank 2002). The fact that the slow outflow can confine the fast wind suggests that the slow outflow carries most of the ejected mass – a conclusion confirmed by Shen & Quataert (2022). Confinement of the initially spherically symmetric fast wind by the dense orbital-plane-concentrated flow gives rise to the bipolar (dumbbell-shaped) morphology often inferred for nova ejecta (e.g. Ribeiro et al. 2013, 2014; Tarasova & Skopal 2016; Naito et al. 2022; Takeda et al. 2022. but see also counter-examples presented by Santamaría et al. 2022). The interface between the slow orbital-plane-concentrated flow and the fast wind is a natural shock formation site. Alternatively, the shock may be located close to the white dwarf, as suggested by the report of 544.8 s periodicity in the γ-ray emission of V5856 Sgr by Li (2022).

The absence of fast variability in the *NuSTAR* X-ray data on V1674 Her dominated by shock-heated plasma (Section 3.1.1) suggests that the shocked region is large and located far away from the white dwarf. The shock velocity ($v_{\rm shock}$) can be related to the post-shock temperature:

$$\mathrm{k}T_{\rm shock} = \frac{3}{16}\mu m_p v_{\rm shock}^2 \quad (3)$$

(equation [6.58] of Dyson & Williams 1997), where $m_{\rm p}$ is the proton mass, k is the Boltzmann constant, and μ is the mean molecular weight. For a fully ionized gas with the abundances derived for V906 Car by Sokolovsky et al. (2020), $\mu = 0.74$. Together with $\mathrm{k}T_{\rm shock} = 4$ keV (Table 1), this corresponds to $v_{\rm shock} \simeq 1700$ km s^{-1}. Taking 10 ks as the variability time-scale in the *NuSTAR* band (Fig. 2), the corresponding length-scale of the shocked region would be 10^{12} cm or 0.1 a.u. It is larger than the white dwarf and the accretion disc (Figueira et al. 2018; these could, in principle, be a site of shock formation).

Association of all the hard X-ray emission observed by *NuSTAR* with the shock within the nova ejecta is natural in the context of other *NuSTAR*-observed novae, but is not a trivial conclusion given the IP nature of V1674 Her. The IPs are known for optically thin, spin-modulated X-rays (Norton & Watson 1989) produced in the post-shock region of their accretion columns just above the white dwarf surface. In the case of V1674 Her, however, the spin modulation is detected only in the optically-thick, supersoft component. Accretion powered X-rays of IPs are usually seen to be spin-modulated (Mukai et al. 2015), although not always (see e.g. Coughenour et al. 2022). This may be simply due to the well-known decrease in IP spin modulation amplitude with increasing photon energy (Norton & Watson 1989).

The reason for the X-ray modulation in V1674 Her being confined to soft X-rays might be that, as the white dwarf atmosphere expanded following the nova eruption, the shock within the accretion column formed further away from the white dwarf resulting in lower velocity reached by the infalling material and hence a lower post-shock temperature. Another possibility is enhanced Compton cooling of the accreting material (Frank, King & Raine 2002; Nelson et al. 2011) facilitated by the dense radiation field near the surface of the hydrogen-burning white dwarf.

Depending on the relative masses of the accretion disc and nova ejecta, the accretion disc may survive the eruption or be completely swept away (Drake & Orlando 2010; Figueira et al. 2018). The periodic variations were missing in both optical and X-ray bands near the nova peak (Hansen et al. 2021), either as a result of temporarily arrested accretion or due to the expanded photosphere engulfing the binary system outshining and obscuring the effects of accretion. The orbital and spin modulations emerged in the optical band on day 4 and day 12 after the eruption, respectively (Patterson et al. 2022). If we interpret the spin modulation as the result of accretion (like in the non-

Table 3. V1674 Her luminosity.

Band	Luminosity
γ-ray bright epoch near the optical peak:	
18 h integration 0.1–300 GeV	3.2×10^{36} erg s^{-1}
18 h average bolometric optical	1.5×10^{39} erg s^{-1}
Peak bolometric optical	2.3×10^{39} erg s^{-1}
NuSTAR epoch at $t_0 + 11.3$ d:	
0.1–300 GeV	$<1 \times 10^{36}$ erg s^{-1}
3.0–30 keV	1.0×10^{34} erg s^{-1}
0.3–78 keV	1.4×10^{34} erg s^{-1}
Bolometric optical	9.6×10^{37} erg s^{-1}

nova IPs), that would mean the accretion has restarted by the time of our *NuSTAR* observation. The super-soft X-ray emission modulated with the white dwarf spin period appeared around $t_0 + 18.9$ d (Drake et al. 2021; Page et al. 2021), after our *NuSTAR* observation.

From the X-ray grating spectroscopy by Drake et al. (2021), we know the donor star has non-zero Fe abundance. Therefore, we would expect to see strong Fe lines in the 6–7 keV range (commonly found in IPs; Shaw et al. 2018, Luna et al. 2018, Coughenour et al. 2022, Joshi et al. 2022) had the shocked plasma been accreted from the donor. One could also expect strong intrinsic absorption for accretion-powered X-rays of IPs. In summary, the X-ray emission of V1674 Her observed by *NuSTAR* is likely associated with a shock within the nova ejecta, not accretion on the magnetized white dwarf.

4.3 Distance and luminosity

The progenitor of nova V1674 Her has a negative parallax value reported in the *Gaia* Early Data Release 3, so the distance of $6.0^{+3.8}_{-2.8}$ kpc listed by Bailer-Jones et al. (2021) reflects the prior constructed from a 3Dl model of the Galaxy rather than the actual geometric distance measurement. Therefore, we have to rely on indirect distance indicators to determine the nova luminosity (results summarized in Table 3).

V1674 Her is an IP, and according to Patterson et al. (2022) it brightened from $V = 20.5$. Using $A(V) = 1.7$ mag, the dereddened quiescent magnitude is then $V_0 = 18.8$. In comparison, a normal IP with an orbital period of 3.67 h (Section 2) has a typical $M_V = 4.8$ (with a scatter of 1 magnitude; the majority of IPs are near the absolute V magnitude – orbital period relationship for dwarf novae in outburst of Warner 1987; Mukai et al. in preparation). This implies a distance of $6.3^{+3.8}_{-2.4}$ kpc. A rare low-luminosity IP (that would correspond to the dwarf-novae-in-quiescence relation of Warner 1987) with $P_{\rm orb} = 3.67$ h would have $M_V \sim 8.5$, placing it at 1.1 kpc. Such a small distance is inconsistent with an estimate based on optical extinction: adopting $E(B - V) = 0.55$ mag reported by Munari et al. (2021), we use the 3D Galactic dust map of Bovy et al. (2016) to estimate the distance to V1674 Her, >5 kpc. The ~6.3 kpc distance is also consistent with the angular diameter of the ejecta measured at $t_0 + 2$ d and $t_0 + 3$ d with the CHARA optical interferometer (Schaefer, private communication; ten Brummelaar et al. 2005; Schaefer et al. 2020). We note that Woodward et al. (2021) estimated a smaller distance of 4.7 kpc based on the purported relationship between the absolute magnitude at maximum and the rate of the light curve decline for novae, Schaefer (2022) reported the distance of $3.2^{+2.1}_{-0.8}$ kpc by combining the negative *Gaia* parallax with complex nova-specific priors, while Drake et al. (2021) adopted a nominal distance of 5 kpc in their analysis. We prefer the 6.3 kpc distance based on the expected IP host magnitude, preliminary CHARA expansion parallax, and the lower limit from the 3D Galactic extinction model.

At 6.3 kpc distance, the 3.0–30 keV luminosity of V1674 Her is 1.0×10^{34} erg s^{-1}. The *NuSTAR* band luminosity of V1674 Her is comparable to that of V5855 Sgr (Nelson et al. 2019) and V906 Car (Sokolovsky et al. 2020) and is an order of magnitude larger than the luminosity of YZ Ret (Sokolovsky et al. 2022a). Only an order-of-magnitude comparison is appropriate here, as these novae only have one (two for V906 Car) *NuSTAR* snapshots, while the flux in the *NuSTAR* band is expected to vary with time.

Adopting the brightest visual estimate 6.0 mag. as the peak magnitude of V1674 Her and assuming it to be equivalent to V we follow the procedure detailed by Sokolovsky et al. (2022a) to estimate the peak bolometric flux per unit area (Mamajek et al. 2015)

$$f = 2.518 \times 10^{-5} \times 10^{-0.4(V + \mathrm{BC} - A_V)}\ \mathrm{erg\ cm^{-2}\ s^{-1}}, \tag{4}$$

where BC is the bolometric correction (for the nova at peak we adopt BC = −0.03). At the above mentioned distance this translates to a bolometric luminosity of 2.3×10^{39} erg s^{-1} (absolute magnitude $M = -9.7$).

Taking $V = 11.8$ during the *NuSTAR* observation (Fig. 2), applying a bolometric correction of −2.36 for the *Swift*/UVOT derived temperature (Section 3.2) according to table 3.1 of Budding & Demircan (2007), and correcting for extinction (Section 2), we estimate a bolometric luminosity of 9.6×10^{37} erg s^{-1}. Due to the combined uncertainties in magnitude (typically 0.1 mag. for visual and 0.02 mag for CCD measurements, real variability over the *Fermi* and *NuSTAR* exposures), distance, bolometric correction, and the magnitude-to-flux conversion, the combined uncertainty on the luminosity is expected to be at the tens of per cent level. We also compute monochromatic fluxes at 5500 Å (2.25 eV): $\nu F_\nu = 3.8 \times 10^{-7}$ (peak) and $\nu F_\nu = 1.8 \times 10^{-9}$ erg cm^{-2} s^{-1} (*NuSTAR* epoch) using the magnitude zero points from Bessell, Castelli & Plez (1998).

Overall, the eruption of V1674 Her was well within the normal diversity of classical nova eruptions. This is at odds with the 'micronova' scenario where the nuclear burning is confined to a small region of the white dwarf surface near the magnetic poles (Scaringi et al. 2022a, b, see also Livio, Shankar & Truran 1988 and Shara 1989). The magnetically confined nuclear burning region would produce the soft X-ray spin modulation observed in V1674 Her by Drake et al. (2021) and Lin et al. (2022). A 'micronova' has a peak optical luminosity of 10^{34} erg s^{-1} and eruptions lasting ~10 h (Scaringi et al. 2022b). V1674 Her was among the fastest known novae and may well be at the extreme of the distribution in other ways, too, but it definitely was not a micronova. Had the magnetic field of an IP been capable of confining accreted matter, the eruption of V1674 Her would have been much less energetic. Also, 3 out of the 6 brightest novae of the 20th century are firmly established to be magnetic – DQ Her (Walker 1956), GK Per (Norton, Watson & King 1988), and V1500 Cyg (Stockman, Schmidt & Lamb 1988) – and there are quite a few others that were proposed to be magnetic, at various levels of trustworthiness. Normal nova eruptions seem to routinely occur on magnetic white dwarfs.

4.4 The origin of radio emission

V1674 Her remains unresolved in all our VLA observations listed in Table 2. However, by knowing the time of the eruption (t_0), distance, and the nova shell expansion velocity (from optical spectroscopy), we can estimate the shell's angular size. Then, together with the observed total flux density, we can constrain the surface brightness of the radio emission – i.e. the brightness temperature, T_b. The brightness temperature of thermal emission cannot exceed the physical temperature of the emitting body (equation 12) while the synchrotron T_b can reach 10^{11} K (Kellermann & Pauliny-Toth 1969; Readhead 1994). By comparing the estimated T_b with a knowledge of the emitter's physical temperature, one can determine if the observed emission is consistent with being thermal. Following e.g. Nyamai et al. (2021) we calculate

$$T_b = 1222 \times \left(\frac{\nu}{1\,\mathrm{GHz}}\right)^{-2} \times \left(\frac{F_\nu}{1\,\mathrm{mJy}}\right) \times \left(\frac{\theta}{1\,\mathrm{arcsec}}\right)^{-2}\,\mathrm{K}, \qquad (5)$$

where ν is the observing frequency, F_ν is the spectral flux density, and θ is the FWHM of a source that is assumed to have a Gaussian shape. The difference between the coefficients in equation (5) and equation (11) arises from the different meaning of θ. While in equation (5) we use the θ definition common in radio astronomy observations, in equation (11) θ is the angular diameter of a circle having the surface area $\ln 2 \times$ that of a Gaussian source with FWHM $= \theta$. This $\ln 2$ factor is unimportant for the following order-of-magnitude discussion of T_b.

Adopting an expansion velocity of 3500 km s^{-1} from Aydi et al. (2021) and the distance from Section 4.3, we use equation (5) to calculate the lower limit on T_b at each VLA epoch. The lowest T_b values are achieved when the observed radio emission covers the whole expanding ejecta, rather than a few compact knots.

The first few detections of V1674 Her at 13.7 to 34.9 GHz have the estimated lower limit $T_b >$ afew $\times\ 10^4$ K (Fig. 7), consistent with the expected effective temperature of nova ejecta photoionized by the central nuclear-burning white dwarf (Cunningham, Wolf & Bildsten 2015). While the white dwarf atmosphere is very hot (10^5–10^6 K; Wolf et al. 2013; Cunningham et al. 2015) producing super-soft X-ray emission, the photoionized ejecta are cooled by forbidden line emission down to an equilibrium temperature of $\sim 10^4$ K (Dyson & Williams 1997; Proxauf, Öttl & Kimeswenger 2014).

The estimated T_b lower limit values rise steeply around $t_0 + 10.1$ d and reach $\gtrsim 10^5$ K by $t_0 + 13.1$ d at and below 16.5 GHz (Fig. 7). The high peak T_b values suggest a non-thermal origin of the radio emission near its peak. In Section 4.5 we discuss why the fraction of the nova shell shock-heated to $\sim 10^7$ K (that we observe with *NuSTAR*) cannot be responsible for a significant fraction of the radio emission (and absorption) observed with the VLA.

The final argument supporting a non-thermal origin of the radio emission peak is the fast rise of the radio flux density. The dashed line in the middle panel of Fig. 7 indicates $F_\nu \propto t^2$, the rate at which the flux density of a uniformly expanding, constant temperature, optically thick cloud should increase (e.g. Seaquist & Bode 2008).

The conclusion about the likely synchrotron origin of most of V1674 Her's radio emission does not contradict the e-EVN 1.6 GHz upper limit of 36 μJy beam^{-1} on 2021-06-22 ($t_0 + 10$ d) reported by Paragi et al. (2021). The total flux density observed by the VLA on that day (Fig. 8) extrapolated to 1.6 GHz is well below the reported limit. One could speculate that had the e-EVN observation been conducted at least a few days later, it could have resulted in a positive detection.

The radio spectrum of V1674 Her evolves from steeply inverted ($\alpha = 1.4 - 1.7$) to flat with a sign of curvature. The optically thin synchrotron spectrum cannot have a slope greater than $\alpha = +1/3$ for any energy distribution of the emitting electrons as the synchrotron spectrum of a single electron has no region rising faster than $F_\nu \propto \nu^{+1/3}$ (Ginzburg & Syrovatskii 1965; Kellermann 1966; Ginzburg 1979). The optically thin thermal free-free (bremsstrahlung) emission slope is $F_\nu \propto \nu^{-0.1}$ (Pacholczyk 1970). Therefore, at early times, the shape of the spectrum is determined by optical depth effects. The spectral slope, however, never reaches the canonical $\alpha = +2.5$ of a source experiencing synchrotron self-absorption (Pacholczyk 1970) or $\alpha = +2$ of an optically thick thermal source (Ghisellini 2013). The optically thick spectral slope that is more shallow than the canonical values may arise from the source being inhomogeneous. For a thermal source, the slope of $\alpha = +2$ is expected in the idealized case of an infinitely steep drop-off in density at the outermost edge of the source. A power-law drop-off in density with distance from the source centre, $n \propto r^{-8}$, would account for $\alpha = +1.7$ for a thermal bremsstrahlung source.

According to Kellermann (1966), free-free absorption of optically thin synchrotron emission with $F_\nu = A\nu^\alpha$ will result in an exponential drop at low frequencies, $F_\nu = A\nu^\alpha e^{-(\nu_{\tau=1}/\nu)^2}$ in the case of an external screen (an absorber located between the emitter and observer), and a modified power-law spectrum $F_\nu = \frac{A}{\nu^2_{\tau=1}}\nu^{\alpha+2}$ if the absorber is mixed with the synchrotron-emitting plasma. Here, $\nu_{\tau\,=\,1}$ is the frequency at which optical depth is equal to unity, A is a constant, and it is assumed that we can neglect the thermal emission of the absorbing plasma. As with the 'cosmic conspiracy' producing flat spectra of cores in extragalactic radio sources (Blandford & Königl 1979; Marscher 1980; Konigl 1981), the likely explanation of the V1674 Her radio spectrum slope is that there is a gradient of physical properties across the radio emitting region. The change in slope reflects the changes of these properties in time or over the source, as the outer regions of the source become transparent and the inner source regions become visible.

At late epochs, the T_b estimates are consistent with thermal emission (Fig. 7). One may wonder if the synchrotron emission is dominating the peak of the radio light curve but is overtaken by thermal emission later. Two considerations disfavor this possibility. First, the decline from the maximum T_b appears smooth and gradual, with no abrupt change in the decline rate that could suggest change in the dominating emission mechanism (Fig. 7). Second, the latest VLA epoch with a positive detections of V1674 Her (2021-11-01, t_0 + 142.8; Fig. 8) reveals a curved spectrum with a high-frequency spectral index of $\alpha_{\mathrm{sync}} = -0.5 \pm 0.1$, which is < -0.1 – indicative of synchrotron emission.

If we take the radio spectrum peak parameters from this last-detection epoch (Fig. 8), the angular diameter at this epoch (90 mas, estimated earlier for the T_b calculation), and naively apply equation (2) of Marscher (1983) describing a uniform synchrotron cloud, we end up with an unrealistically high magnetic field needed to produce the observed spectral turnover via synchrotron self-absorption. This supports the conclusion of Vlasov, Vurm & Metzger (2016) that it is the free-free opacity that is dominating the radio spectral evolution in novae, irrespective of the emission mechanism (thermal or synchrotron; see also Kantharia et al. 2016 for a discussion of embedded novae). The synchrotron self-absorption spectrum fits to the late VLA epochs in Fig. 8 appear to be just a convenient peaked function that happens to fit the data well with no physical meaning.

There is another mechanism that may attenuate the synchrotron spectrum at low frequencies in the presence of a thermal plasma in the emitting region: the Razin–Tsytovich effect (Ginzburg & Syrovatskii 1965; Kellermann 1966; Rybicki & Lightman 1979). It has been proposed as the reason for the inverted cm-band spectrum of the nova QU Vul by Taylor et al. (1987). The condition $\nu_{\mathrm{RTpeak}} = 20 n_e/B$ (where the peak frequency ν_{RTpeak} is in Hz, the electron density n_e is in cm^{-3} and the magnetic field strength B is in Gauss) for $\nu_{\mathrm{RTpeak}} = 7$ GHz (the lowest radio spectrum peak frequency observed in V1674 Her on $t_0 + 142.8$ d; Fig. 8) implies a density $n_e = 3.5 \times 10^8 B$. This may not be unreasonable for a shocked nova shell (Taylor et al. 1987; Vlasov et al. 2016, c.f. Section 4.5) depending on the assumed magnetic field strength. The spectral index resulting from the Razin–Tsytovich effect is frequency-dependent and is ultimately steeper than that of a self-absorbed source (according to figure 1 of Kellermann 1966), in contrast to the relatively shallow spectral indices of V1674 Her.

Synchrotron emission in novae has been identified before on the basis of high estimated T_b of V809 Cep (Babul et al. 2022), V392 Per, V357 Mus, V5855 Sgr, V5668 Sgr, V2672 Oph, V2491 Cyg, V838 Her, V1500 Cyg (Chomiuk et al. 2021b), helium nova V445 Pup (Nyamai et al. 2021), V906 Car (Aydi et al. 2020a), V1324 Sco (Finzell et al. 2018), V1723 Aql (Weston et al. 2016a), 5589 Sgr (Weston et al. 2016b), V959 Mon (Chomiuk et al. 2014) and QU Vul (Taylor et al. 1987), and via direct VLBI imaging of V959 Mon (Yang et al. 2014), V1674 Her itself (Linford and Williams, private communication) and the embedded (red giant donor) novae RS Oph (Taylor et al. 1989; O'Brien et al. 2006; Rupen, Mioduszewski & Sokoloski 2008; Sokoloski, Rupen & Mioduszewski 2008; Eyres et al. 2009; Munari et al. 2022; de Ruiter et al. 2023), V407 Cyg (Giroletti et al. 2020), and V1535 Sco (Linford et al. 2017). Synchrotron emission was also reported in embedded novae V745 Sco (Kantharia et al. 2016) and V3890 Sgr (Nyamai et al. 2023). A special case is the long-lived synchrotron-emitting remnant of the 1901 nova GK Per that apparently erupted within a planetary nebula (Seaquist et al. 1989; Harvey et al. 2016).

4.5 Thermal radio emission from the X-ray emitting plasma

The observed spectrum of a free-free emitting cloud is determined by its temperature, distance and a combination of the electron density and volume of the cloud. There is a degeneracy between the electron density and volume, so a combination of the two values known as the emission measure (EM) is often used in calculations. There are two definitions of EM (e.g. Weston et al. 2016a), the one used in X-ray astronomy:

$$(\mathrm{EM})_{\mathrm{X-ray}} = \int n_e n_i dV, \tag{6}$$

where n_e is the electron number density, n_i is the number density of ions, and V is the volume occupied by the emitting particles. The APEC plasma emission model normalization, $\mathcal{E}$, provides the volume emission measure of the plasma scaled by the distance (Arnaud et al. 2011):

$$\mathcal{E} = \frac{10^{-14}}{4\pi D_{\mathrm{cm}}^2} (\mathrm{EM})_{\mathrm{X-ray}}, \tag{7}$$

where D_{cm} is distance to the emitting cloud in cm.

Another definition of the emission measure is commonly used in radio astronomy (e.g. Pacholczyk 1970):

$$(\mathrm{EM})_{\mathrm{radio}} = \int n_e n_i dl, \tag{8}$$

where the integration is done along the line of sight crossing the cloud, l, not the cloud volume as in the X-ray definition. To relate $(\mathrm{EM})_{\text{X-ray}}$ to $(\mathrm{EM})_{\mathrm{radio}}$, we have to assume some specific geometry of the cloud. For simplicity, we assume the cloud to be a uniform cylindrical slab (the shape of a ice hockey puck; Fig. 9) of radius r and depth l along the line of sight:

$$(\mathrm{EM})_{\mathrm{X-ray}} = \pi r^2 (\mathrm{EM})_{\mathrm{radio}}. \tag{9}$$

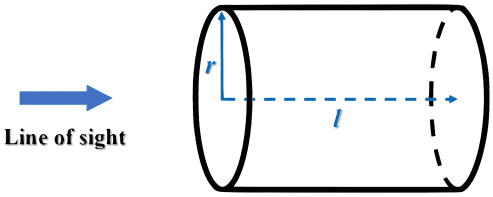

Figure 9. The assumed cylindrical slab geometry of the cloud.

Note that $(\mathrm{EM})_{\text{X-ray}}$ is often expressed in units of cm^{-3}, while $(\mathrm{EM})_{\mathrm{radio}}$ is in pc cm^{-6} – the value of $(\mathrm{EM})_{\mathrm{radio}}$ obtained from equation (9) needs to be divided by the number of centimetres in a parsec to be expressed in the commonly used units. In reality, the emitting region geometry may resemble a sector of a spherical shell with density varying with radius, resulting in an additional factor of a few in the equation relating the two EM values.

From the $(\mathrm{EM})_{\mathrm{radio}}$ and temperature of the emitting cloud, we can calculate the free–free optical depth in the radio band using the approximate relation of Mezger & Henderson (1967):

$$\tau \approx 3.28 \times 10^{-7} \left(\frac{T}{10^4\,\mathrm{K}}\right)^{-1.35} \left(\frac{\nu}{1\,\mathrm{GHz}}\right)^{-2.1} \left(\frac{(\mathrm{EM})_{\mathrm{radio}}}{1\,\mathrm{pc\,cm^{-6}}}\right). \tag{10}$$

For the $(\mathrm{EM})_{\text{X-ray}}$ and temperature (both derived from the *NuSTAR* spectrum, Section 3.1.2) and assuming linear expansion of r starting at t_0 with the optical spectroscopy-derived velocity (Section 4.4), the resulting $(\mathrm{EM})_{\mathrm{radio}} = 3.8 \times 10^8$ pc cm^{-6} for the assumed cylindrical geometry (Fig. 9). The implied optical depth is in the range $\tau = 10^{-3}$–10^{-6} for $\nu = 1$ to 30 GHz. This suggests that the X-ray emitting plasma cannot be responsible for the *absorption* of cm-band radio waves. The absorption may be provided by another cooler component of the plasma located in the foreground of the radio emitting region.

To find out if the X-ray emitting plasma is responsible for the observed radio *emission* we use the convenient equation (1.7) of Weston (2016) to calculate the radio flux density

$$F_\nu = \frac{T_b}{1763\,\mathrm{K}} \left(\frac{\nu}{1\,\mathrm{GHz}}\right)^2 \left(\frac{\theta}{1\,\mathrm{arcsec}}\right)^2 \mathrm{mJy}, \tag{11}$$

where

$$T_b = (1 - e^{-\tau})T \tag{12}$$

is the brightness temperature related to the physical (electron) temperature, T, through the optical depth, τ, that we derive from equation (10), see e.g. Rybicki & Lightman (1979) or Snell, Kurtz & Marr (2019). The predicted $F_\nu \approx 2\,\mu$Jy at cm wavelengths – well below the sensitivity limit of our snapshot VLA observations.

4.6 Ejecta mass constraints

Fast novae are associated with massive white dwarfs and low ejecta masses. At a given accretion rate, the higher surface gravity and smaller surface area of a massive white dwarf facilitate earlier ignition of the thermonuclear runaway, resulting in a smaller amount of ejected material. If the fractional change of 10^{-4} between V1674 Her's pre- and post-eruption white dwarf spin period is attributed to the mass loss via a magnetized wind, this would require mass-loss of 10^{-5}–10^{-4} M$_\odot$ according to Drake et al. (2021). The authors also point out that a large ejecta mass of 10^{-4} M$_\odot$ was reported for another fast nova, V838 Her, by Vanlandingham et al. (1996).

In the following, we constrain the ejecta mass of V1674 Her using the information about the X-ray emission, X-ray absorption, and thermal radio emission. The amount of X-ray emission probes the shock-heated plasma while the X-ray absorption and radio emission independently probe the colder photoionized fraction of the ejecta. All these estimates point to a low ejecta mass (and hence alternative explanations for the spin period change; Section 2); however, the estimates are highly model-dependent.

4.6.1 Minimum ejecta mass from thermal radio emission

The majority of novae produce thermal radio emission (Chomiuk et al. 2021b). Emission from the hot white dwarf photo-ionizes nova ejecta causing it to produce free–free radio emission as it expands. How and when the free-free emission in the radio band changes from optically thick to optically thin is determined by the ejecta mass (Cunningham et al. 2015). We can put constraints on the mass of the ejecta in V1674 Her if a fraction of its radio emission is thermal in origin (e.g. Hjellming 1996; Weston et al. 2016a).

In the radio light curves of novae, where the thermal and synchrotron peaks can be separated, the synchrotron peak typically precedes the thermal peak (Weston et al. 2016a; Finzell et al. 2018; Chomiuk et al. 2021b). In contrast to this tendency, the T_b history (Fig. 7) suggests that thermal radio emission may have dominated the radio light curve of V1674 Her at *early* times, before $t_0 + 10$ d.

By $t_0 + 10$ d the radio spectrum appears slightly curved (Fig. 8), suggesting the optical depth might be starting to drop. From equation (10) and the condition $\tau > 1$ at 13 GHz, we derive $(\mathrm{EM})_{\mathrm{radio}} > 2.1 \times 10^{27}\,\mathrm{cm}^{-5}$ assuming $T = 10^4$ K (unshocked photoionized ejecta).

The thermal radio light curves of novae are often described with the 'Hubble flow' model (Hjellming et al. 1979; Hjellming 1996; Heywood et al. 2005); see appendix A of Finzell et al. (2018). The ejecta are assumed to be in a spherical shell with an inner radius expanding with velocity $v_{\min}$ and an outer radius expanding with $v_{\max}$ resulting in $n \propto r^{-2}$ density profile. Assuming the shell ejected at t_0 with $v_{\max} = 5000\,\mathrm{km\,s^{-1}}$ (the maximum velocity reported by Aydi et al. 2021) and $v_{\min} = 0.1\,v_{\max}$, we find that the $(\mathrm{EM})_{\mathrm{radio}}$ constraint corresponds to an ejecta mass of $> 10^{-7}\,\mathrm{M}_{\odot}$ (if the 13 GHz emission at $t_0 + 10$ is mostly thermal).

4.6.2 Upper limit on the ejecta mass from the absence of intrinsic X-ray absorption

Following Sokolovsky et al. (2020) and Nelson et al. (2021) we estimate the mass of unshocked ejecta by assuming the X-rays originating deep within the ejecta are absorbed by the spherical 'Hubble flow' shell. Taking the same model parameters as for the radio-emission-based mass estimation in Section 4.6.1 and assuming that an intrinsic absorption of $N_{\mathrm{H}} = 10^{21}\,\mathrm{cm}^{-2}$ would have been detectable in our *NuSTAR* plus *Swift*/XRT observations (Sections 3.1.2 and 3.2) we obtain an upper limit on the ejecta mass of a few $\times\ 10^{-7}\mathrm{M}_{\odot}$, close to the thermal radio lower limit.

The absence of detectable intrinsic absorption is inconsistent with a larger ejecta mass of $\times\ 10^{-4}\mathrm{M}_{\odot}$ that would produce an absorbing column of $N_{\mathrm{H}} = 5 \times 10^{23}\,\mathrm{cm}^{-2}$ at day 12 with the above model parameters. The caveat here is that the X-ray upper limit on the unshocked ejecta mass strongly depends on the assumptions of spherical symmetry of the absorber and the minimum expansion velocity of the 'Hubble flow' model (the slower moving material provides most absorption as it remains dense for a longer time).

4.6.3 The mass of X-ray emitting plasma

In order to estimate the density and total mass of the X-ray emitting material we assume the simple cylindrical shape of the emitting region (as in Section 4.5) with the height equal to its radius (geometry used by Taylor et al. 1989). Under this assumption, the observed $(\mathrm{EM})_{\mathrm{X\text{-}ray}}$ value corresponds to the density of $n \sim 10^6\,\mathrm{cm}^{-3}$. Multiplying this by the mean molecular weight appropriate for the nova ejecta (Section 4.2), the proton mass and the cylinder volume we get the total mass of the X-ray emitting plasma to be $10^{-7}\mathrm{M}_{\odot}$. We stress that the above values of mass and density are nothing more than an indication of where in the parameter space the true values might lay. The actual values depend critically on the geometry and density distribution of the shocked ejecta. Specifically, we assumed that the plasma is distributed uniformly across the cylindrical volume (has a filling factor of unity). This mass estimate refers to the shock-heated material which is, presumably, a small part of the ejecta.

4.7 V1674 Her and our understanding of novae

It has long been argued on the basis of optical light curves and spectral evolution that there is no fundamental difference between fast and slow novae (McLaughlin 1939a, b, c). The observation that V1674 Her, being one of the fastest novae ever seen in the Galaxy (Section 2), produces γ-ray and X-ray emitting shocks similar to the ones found in slower novae suggests this is also true for the structure of nova ejecta. The structures within the ejecta responsible for the shock formation, likely the slow equatorial outflow and fast omnidirectional wind (Chomiuk et al. 2014; Shen & Quataert 2022, Section 4.2), must be present in V1674 Her. It does not appear to be the case that a fast nova is dominated by the fast wind while the ejecta of a slow nova is mostly the slow equatorial outflow. Instead, both structures must be present in the fast-evolving V1674 Her, while the time-scale of their interaction is compressed compared to most other novae.

The extreme properties of V1674 Her challenge our understanding of nova outflows and specifically the 'slow torus – fast bipolar wind' scenario (Sections 1 and 4.2). It is tempting to attribute the shock velocity $v_{\mathrm{shock}} \simeq 1700\,\mathrm{km\,s^{-1}}$ (corresponding to $\mathrm{k}T_{\mathrm{shock}} = 4$ keV) to the shock between the early $3500\,\mathrm{km\,s^{-1}}$ and late $5000\,\mathrm{km\,s^{-1}}$ outflows seen in optical spectra by Aydi et al. (2021). Even if the shock is between the $3500\,\mathrm{km\,s^{-1}}$ outflow and a slower ejecta not seen in spectroscopy, that would still imply the slow torus velocity of $>1000\,\mathrm{km\,s^{-1}}$. This is considerably faster than the expected orbital velocity of the binary companion, suggesting that it is unlikely that the common envelope interaction was the mechanism responsible for the slow torus ejection in V1674 Her (Chomiuk et al. 2021a). Another challenge for the common envelope ejection origin of the shocked material is the six-hour delay between the start of the eruption (t_0) and the onset of γ-ray emission (Section 3.3, Fig. 1). It would be surprising if less than two orbital revolutions (3.67 h period) are sufficient to eject the common envelope.

An onset of γ-rays delayed by a few days from the optical rise is commonly observed in slower novae (Ackermann et al. 2014; Cheung et al. 2016; Munari et al. 2017). While such a delay is naturally expected in the two-flow scenario, the alternative possibility is that if γ-rays are produced simultaneously with the optical rise, they may have a hard time escaping the system due to photo-nuclear or $\gamma\gamma$ pair production opacity (Metzger et al. 2016; Martin et al. 2018; Fang et al. 2020; H. E. S. S. Collaboration 2022).

The correlated variations in optical and γ-ray flux observed in V5856 Sgr by Li et al. (2017) and V906 Car by Aydi et al. (2020a) revealed that a significant fraction of nova optical light might be shock-powered. Munari et al. (2017) suggested that in addition to the main optical light-curve peak associated with the greatest expansion of the photosphere (common to all novae) there might be a separate peak in the light curves of GeV-bright novae associated with optical emission of the γ-ray-producing shocks. The light curve of V1674 Her has a single peak. However a kink in the optical light curve is hinted around the time the γ-ray emission ended ($t_0 + 1$ d; the rate of decline has decreased). One may speculate that shocks could have contributed to the optical light before $t_0 + 1$ d producing an additional bump right on top of the common 'fireball' light curve peak.

Detection of the GeV γ-rays before the optical peak (Fig. 1) is at odds with the prediction of the 'continuously changing velocity wind' model of Hachisu & Kato (2022). However, one may overcome this contradiction if the optical peak is prolonged by the contribution of shock-powered optical light.

5 CONCLUSIONS

We conducted a joint analysis of γ-ray (*Fermi*-LAT), X-ray (*NuSTAR*, *Swift*/XRT), optical (AAVSO, Evryscope, ASAS-SN), and radio (VLA) observations of an exceptionally fast Galactic nova V1674 Her.

(i) V1674 Her was clearly detected by *Fermi*-LAT, but only for the duration of 18 h near the optical peak. There is a delay of about 6 h between the onset of optical and detectable γ-ray emission. The shape and the cut-off energy of the γ-ray spectrum are poorly constrained taking into account the limited statistics.

(ii) The *NuSTAR* spectrum of V1674 Her is consistent with having been produced by shock-heated plasma with non-solar elemental abundances. It is remarkably similar to the spectra of three classical novae previously detected by *NuSTAR*. The lack of periodic variability in the hard X-ray flux at the spin period of the white dwarf suggests that the *NuSTAR*-detected X-rays from V1674 Her are associated with a shock within the nova ejecta, not accretion on the magnetized white dwarf.

(iii) Given the strong similarity between the high-energy properties of V1674 Her and those of other classical novae in the days to weeks after eruption, it appears that neither the exceptionally high speed of this nova, nor the intermediate polar nature of the host system affect the shock development within the ejecta.

(iv) We interpret the radio emission of V1674 Her as being shock-powered synchrotron emission attenuated by free–free absorption. Unlike many other novae, V1674 Her displayed weak thermal radio emission that contributed before the synchrotron emission reached its peak.

(v) The radio emission (Section 4.6.1) and X-ray emission and absorption (Section 4.6.2) point to a low ejecta mass of $\sim 10^{-7}$ $M_{\odot}$, however the different ejecta mass estimation techniques do not necessarily probe the same parts of the ejecta.

(vi) Being an exceptionally fast nova, V1674 Her might serve as a stress test for the 'slow torus – fast bipolar wind' scenario (outlined in Sections 4.2 and 4.7) of shock formation in novae. For this scenario to hold in V1674 Her, common-envelope action must have been able to eject the envelope very quickly and the fast flow must have begun before the detection of γ-rays within 6 h of t_0.

ACKNOWLEDGEMENTS

We acknowledge with thanks the variable star observations from the AAVSO International Database contributed by observers worldwide and used in this research. We thank Elizabeth O. Waagen and Dr Brian K. Kloppenborg for their assistance in communicating with the AAVSO observers and Dr Nikolai N. Samus for the help in gathering information about the circumstances surrounding the discovery of V1674 Her.

This paper made use of data from the *NuSTAR* mission, a project led by the California Institute of Technology, managed by the Jet Propulsion Laboratory, funded by the National Aeronautics and Space Administration. This research has made use of the *NuSTAR* Data Analysis Software (NuSTARDAS) jointly developed by the ASI Science Data Center (ASDC, Italy) and the California Institute of Technology (USA).

We acknowledge the use of public data from the *Swift* data archive.

The *Fermi* LAT Collaboration acknowledges generous ongoing support from a number of agencies and institutes that have supported both the development and the operation of the LAT as well as scientific data analysis. These include the National Aeronautics and Space Administration and the Department of Energy in the United States, the Commissariat à l'Energie Atomique and the Centre National de la Recherche Scientifique/Institut National de Physique Nucléaire et de Physique des Particules in France, the Agenzia Spaziale Italiana and the Istituto Nazionale di Fisica Nucleare in Italy, the Ministry of Education, Culture, Sports, Science and Technology (MEXT), High Energy Accelerator Research Organization (KEK) and Japan Aerospace Exploration Agency (JAXA) in Japan, and the K. A. Wallenberg Foundation, the Swedish Research Council and the Swedish National Space Board in Sweden.

Additional support for science analysis during the operations phase is gratefully acknowledged from the Istituto Nazionale di Astrofisica in Italy and the Centre National d'Études Spatiales in France. This work performed in part under DOE Contract DE-AC02-76SF00515.

The National Radio Astronomy Observatory is a facility of the National Science Foundation operated under cooperative agreement by Associated Universities, Inc.

This material is based upon work supported by the National Science Foundation under Grants No. AST-1751874 and AST-1816100. We acknowledge support for this work from NASA projects *Fermi* 80NSSC20K1535, *NuSTAR* 80NSSC21K0277, *XMM–Newton* 80NSSC21K0277, and *Swift* 80NSSC21K0173. BDM acknowledges support from NASA under Grant No. 80NSSC22K0807. KLP acknowledges support from the UK Space Agency. IV acknowledges support by the ETAg grant PRG1006 and by EU through the ERDF CoE grant TK133. This work was supported by the European Research Council, ERC Starting grant *MessMapp*, S.B. Principal Investigator, under contract no. 949555. Research at the Naval Research Laboratory is supported by NASA DPR S-15633-Y. This work made use of ASTROPY: a community-developed core Python package and an ecosystem of tools and resources for astronomy (Astropy Collaboration 2013, 2018, 2022). This research made use of PHOTUTILS, an ASTROPY package for detection and photometry of astronomical sources (Bradley et al. 2022).

DATA AVAILABILITY

The raw *Fermi*-LAT, *NuSTAR*, *Swift*, AAVSO, ASAS-SN, and VLA data are available at the respective archives. The readers are encouraged to contact the authors for processed data and analysis details. The data files and plotting scripts corresponding to Figs. 1, 2, 3, 4, 7, 8, and Table 1 may be found at https://kirx.net/~kirx/V1674_Her__public_data/ and http://scan.sai.msu.ru/~kirx/data/V1674_Her__public_data/

REFERENCES

Abbasi R. et al., 2022, preprint (arXiv:2212.06810)
Abdo A. A. et al., 2010, Science, 329, 817
Abdollahi S. et al., 2020, ApJS, 247, 33
Acciari V. A. et al., 2022, Nat. Astron., 6, 689
Ackermann M. et al., 2014, Science, 345, 554
Albert A. et al., 2022, ApJ, 940, 141
Arnaud K. A., 1996, in Jacoby G. H., Barnes J., eds, ASP Conf. Ser. Vol. 101, Astronomical Data Analysis Software and Systems V. Astron. Soc. Pac., San Francisco, p. 17
Arnaud K., Smith R., Siemiginowska A., 2011, Handbook of X-ray Astronomy. Cambridge Univ. Press, Cambridge
Asplund M., Grevesse N., Sauval A. J., Scott P., 2009, ARA&A, 47, 481
Astropy Collaboration, 2013, A&A, 558, A33
Astropy Collaboration, 2018, AJ, 156, 123
Astropy Collaboration, 2022, ApJ, 935, 167
Atwood W. B. et al., 2009, ApJ, 697, 1071
Atwood W. et al., 2013, preprint (arXiv:1303.3514)
Aydi E. et al., 2020a, Nat. Astron., 4, 776
Aydi E. et al., 2020b, ApJ, 905, 62
Aydi E. et al., 2021, Astron. Telegram, 14710, 1
Babul A.-N. et al., 2022, MNRAS, 515, 3028
Bailer-Jones C. A. L., Rybizki J., Fouesneau M., Demleitner M., Andrae R., 2021, AJ, 161, 147
Balick B., Frank A., 2002, ARA&A, 40, 439
Balman Ş., 2020, Adv. Space Res., 66, 1097
Balucinska-Church M., McCammon D., 1992, ApJ, 400, 699
Bath G. T., Shaviv G., 1976, MNRAS, 175, 305
Bessell M. S., Castelli F., Plez B., 1998, A&A, 333, 231
Blandford R. D., Königl A., 1979, ApJ, 232, 34
Bode M. F., Evans A., 2008, Classical Novae. Cambridge Univ. Press, Cambridge
Bovy J., Rix H.-W., Green G. M., Schlafly E. F., Finkbeiner D. P., 2016, ApJ, 818, 130
Bradley L. et al., 2022, astropy/photutils: 1.5.0, Zenodo
Brickhouse N. S., Desai P., Hoogerwerf R., Liedahl D. A., Smith R. K., 2005, in Smith R., ed., AIP Conf. Ser. Vol. 774, X-ray Diagnostics of Astrophysical Plasmas: Theory, Experiment, and Observation. Am. Inst. Phys., New York, p. 405
Bruel P., Burnett T. H., Digel S. W., Johannesson G., Omodei N., Wood M., 2018, preprint (arXiv:1810.11394)
Buckley D. A. H., 2000, New Astron. Rev., 44, 63
Budding E., Demircan O., 2007, Introduction to Astronomical Photometry, Cambridge Observing Handbooks for Research Astronomers Vol. 6. Cambridge Univ. Press, Cambridge
Burrows D. N. et al., 2005, Space Sci. Rev., 120, 165
Caprioli D., Spitkovsky A., 2014, ApJ, 783, 91
Cardelli J. A., Clayton G. C., Mathis J. S., 1989, ApJ, 345, 245
Casanova J., José J., García-Berro E., Shore S. N., Calder A. C., 2011, Nature, 478, 490
Casanova J., José J., García-Berro E., Shore S. N., 2016, A&A, 595, A28
Casanova J., José J., Shore S. N., 2018, A&A, 619, A121
Chandra P., 2018, Space Sci. Rev., 214, 27
Cheung C. C. et al., 2016, ApJ, 826, 142
Cheung C. C. et al., 2022, ApJ, 935, 44
Chomiuk L. et al., 2014, Nature, 514, 339
Chomiuk L., Metzger B. D., Shen K. J., 2021a, ARA&A, 59, 391
Chomiuk L. et al., 2021b, ApJS, 257, 49
Coughenour B. M., Tomsick J. A., Shaw A. W., Mukai K., Clavel M., Hare J., Krivonos R., Fornasini F. M., 2022, MNRAS, 511, 4582
Cunningham T., Wolf W. M., Bildsten L., 2015, ApJ, 803, 76
Darnley M. J. et al., 2016, ApJ, 833, 149
Das R., 2021, J. Astrophys. Astron., 42, 13
De K. et al., 2021, ApJ, 912, 19
de Diego J. A., 2010, AJ, 139, 1269
de Jager O. C., Büsching I., 2010, A&A, 517, L9
de Jager O. C., Raubenheimer B. C., Swanepoel J. W. H., 1989, A&A, 221, 180
de Martino D., Bernardini F., Mukai K., Falanga M., Masetti N., 2020, Adv. Space Res., 66, 1209
de Ruiter I., Nyamai M. M., Rowlinson A., Wijers R. A. M. J., O'Brien T. J., Williams D. R. A., Woudt P., 2023, preprint (arXiv:2301.10552)
Delgado L., Hernanz M., 2019, MNRAS, 490, 3691
Della Valle M., Izzo L., 2020, A&AR, 28, 3
Denissenkov P. A., Herwig F., Bildsten L., Paxton B., 2013, ApJ, 762, 8
Drake J. J., Orlando S., 2010, ApJ, 720, L195
Drake J. J. et al., 2021, ApJ, 922, L42
Duerbeck H. W., 1987, The Messenger, 50, 8
Dyson J. E., Williams D. A., 1997, The Physics of the Interstellar Medium. Institute of Physics Publishing, Bristol
Eyres S. P. S. et al., 2009, MNRAS, 395, 1533
Fang K., Metzger B. D., Vurm I., Aydi E., Chomiuk L., 2020, ApJ, 904, 4
Fermi Science Support Development Team, 2019, Astrophysics Source Code Library, record ascl:1905.011
Figueira J., José J., García-Berro E., Campbell S. W., García-Senz D., Mohamed S., 2018, A&A, 613, A8
Finzell T. et al., 2018, ApJ, 852, 108
Franckowiak A., Jean P., Wood M., Cheung C. C., Buson S., 2018, A&A, 609, A120
Frank J., King A., Raine D. J., 2002, Accretion Power in Astrophysics, 3rd edn. Cambridge Univ. Press, Cambridge
Friedjung M., 2011, A&A, 536, A97
Gaia Collaboration, 2016, A&A, 595, A1
Gaia Collaboration, 2022, preprint (arXiv:2208.00211)
Galiullin I. I., Gilfanov M. R., 2021, Astron. Lett., 47, 587
Gehrels N., 1997, Nuovo Cimento B Ser., 112B, 11
Gehrels N. et al., 2004, ApJ, 611, 1005
Gehrz R. D., Truran J. W., Williams R. E., Starrfield S., 1998, PASP, 110, 3
Ghisellini G., 2013, Radiative Processes in High Energy Astrophysics, Vol. 873. Springer, Cham, Switzerland
Ginzburg V. L., 1979, Theoretical Physics and Astrophysics. Pergamon, Oxford
Ginzburg V. L., Syrovatskii S. I., 1965, ARA&A, 3, 297
Giroletti M. et al., 2020, A&A, 638, A130
Gomez-Gomar J., Hernanz M., Jose J., Isern J., 1998, MNRAS, 296, 913
Gordon A. C., Aydi E., Page K. L., Li K.-L., Chomiuk L., Sokolovsky K. V., Mukai K., Seitz J., 2021, ApJ, 910, 134
Greisen E. W., 2003, in Heck A. ed., Astrophysics and Space Science Library, Vol. 285, Information Handling in Astronomy – Historical Vistas. Springer-Verlag, Berlin, p. 109
Guetta D., Hillman Y., Della Valle M., 2023, J. Cosmol. Astropart. Phys., 2023, 015
Guo Y., Wu C., Wang B., 2022, A&A, 660, A53
Güver T., Özel F., 2009, MNRAS, 400, 2050
H. E. S. S. Collaboration, 2022, Science, 376, 77
HEASARC, 2014, Astrophysics Source Code Library, record ascl:1408.004
HI4PI Collaboration, 2016, A&A, 594, A116
Hachisu I., Kato M., 2022, ApJ, 939, 1
Hansen K. Y. et al., 2021, Res. Notes Am. Astron. Soc., 5, 244
Harrison F. A. et al., 2013, ApJ, 770, 103
Harvey E., Redman M. P., Boumis P., Akras S., 2016, A&A, 595, A64
Helton L. A. et al., 2012, ApJ, 755, 37
Hernanz M., Sala G., 2010, Astron. Nachr., 331, 169
Heywood I., O'Brien T. J., Eyres S. P. S., Bode M. F., Davis R. J., 2005, MNRAS, 362, 469
Hjellming R. M., 1996, in Taylor A. R., Paredes J. M., eds, ASP Conf. Ser. Vol. 93, Radio Emission from the Stars and the Sun. Astron. Soc. Pac., San Francisco, p. 174
Hjellming R. M., Wade C. M., Vandenberg N. R., Newell R. T., 1979, AJ, 84, 1619
Hoard D. W. et al., 2014, ApJ, 786, 68
Högbom J. A., 1974, A&AS, 15, 417

Imbriani G. et al., 2004, A&A, 420, 625
Ivanova N. et al., 2013, A&AR, 21, 59
Joshi A., Wang W., Pandey J. C., Singh K. P., Naik S., Raj A., Anupama G. C., Rawat N., 2022, A&A, 657, A12
Joye W. A., Mandel E., 2003, in Payne H. E., Jedrzejewski R. I., Hook R. N., eds, ASP Conf. Ser. Vol. 295, Astronomical Data Analysis Software and Systems XII. Astron. Soc. Pac., San Francisco, p. 489
Kafka S., 2021, Observations from the AAVSO International Database. Available at https://www.aavso.org
Kalberla P. M. W., Burton W. B., Hartmann D., Arnal E. M., Bajaja E., Morras R., Pöppel W. G. L., 2005, A&A, 440, 775
Kamae T., Karlsson N., Mizuno T., Abe T., Koi T., 2006, ApJ, 647, 692
Kantharia N. G. et al., 2016, MNRAS, 456, L49
Kato M., Hachisu I., 1994, ApJ, 437, 802
Kato M., Saio H., Hachisu I., 2022, ApJ, 935, L15
Kawash A. et al., 2021, ApJ, 910, 120
Kawash A. et al., 2022, ApJ, 937, 64
Kazarovets E. et al., 2021, Central Bureau Electronic Telegrams, 4977
Kellermann K. I., 1966, Austral. J. Phys., 19, 195
Kellermann K. I., Pauliny-Toth I. I. K., 1969, ApJ, 155, L71
Kerr M., 2011, ApJ, 732, 38
Knigge C., Baraffe I., Patterson J., 2011, ApJS, 194, 28
Kochanek C. S. et al., 2017, PASP, 129, 104502
König O. et al., 2022, Nature, 605, 248
Konigl A., 1981, ApJ, 243, 700
Kwok S., 1982, ApJ, 258, 280
LUNA Collaboration, 2006, Phys. Lett. B, 634, 483
Law N. M., Fors O., Wulfken P., Ratzloff J., Kavanaugh D., 2014, in Stepp L. M., Gilmozzi R., Hall H. J., eds, Proc. SPIE Conf. Ser. Vol. 9145, Ground-based and Airborne Telescopes V. SPIE, Bellingham, p. 91450Z
Lee S.-H., Maeda K., Kawanaka N., 2018, ApJ, 858, 53
Li K.-L., 2021a, Astron. Telegram, 14705, 1
Li K.-L., 2021b, Astron. Telegram, 14707, 1
Li K.-L., 2022, ApJ, 924, L17
Li K.-L. et al., 2017, Nat. Astron., 1, 697
Li K.-L., Hambsch F.-J., Munari U., Metzger B. D., Chomiuk L., Frigo A., Strader J., 2020, ApJ, 905, 114
Lin L. C.-C., Fan J.-L., Hu C.-P., Takata J., Li K.-L., 2022, MNRAS, 517, L97
Linford J. D. et al., 2017, ApJ, 842, 73
Lister M. L. et al., 2009, AJ, 137, 3718
Livio M., 1990, in Cassatella A., Viotti R., eds, Proc. IAU Colloq. 122: Physics of Classical Novae, Vol. 369. Springer-Verlag, Berlin, New York, p. 342
Livio M., Soker N., 1988, ApJ, 329, 764
Livio M., Shankar A., Truran J. W., 1988, ApJ, 330, 264
Livio M., Shankar A., Burkert A., Truran J. W., 1990, ApJ, 356, 250
Lloyd H. M., O'Brien T. J., Bode M. F., 1997, MNRAS, 284, 137
Luna G. J. M., Mukai K., Orio M., Zemko P., 2018, ApJ, 852, L8
Luna G. J. M. et al., 2021, Astron. Telegram, 14872, 1
MacDonald J., 1980, MNRAS, 191, 933
MacDonald J., Fujimoto M. Y., Truran J. W., 1985, ApJ, 294, 263
Maccarone T. J., Beardmore A., Mukai K., Page K., Pichardo Marcano M., Rivera Sandoval L., 2021, Astron. Telegram, 14776, 1
Madsen K. K. et al., 2015, ApJS, 220, 8
Madsen K. K., Beardmore A. P., Forster K., Guainazzi M., Marshall H. L., Miller E. D., Page K. L., Stuhlinger M., 2017, AJ, 153, 2
Mamajek E. E. et al., 2015, preprint (arXiv:1510.06262)
Marscher A. P., 1980, Nature, 288, 12
Marscher A. P., 1983, ApJ, 264, 296
Martin A. J. et al., 2018, MNRAS, 475, 1521
Masci F. J. et al., 2019, PASP, 131, 018003
Mattox J. R. et al., 1996, ApJ, 461, 396
McLaughlin D. B., 1939a, Pop. Astron., 47, 410
McLaughlin D. B., 1939b, Pop. Astron., 47, 481
McLaughlin D. B., 1939c, Pop. Astron., 47, 538
McLaughlin D. B., 1956, Vistas Astron., 2, 1477
McMullin J. P., Waters B., Schiebel D., Young W., Golap K., 2007, in Shaw R. A., Hill F., Bell D. J., eds, ASP Conf. Ser. Vol.376, Astronomical Data Analysis Software and Systems XVI. Astron. Soc. Pac., San Francisco, p. 127
Metzger B. D., Pejcha O., 2017, MNRAS, 471, 3200
Metzger B. D., Hascoët R., Vurm I., Beloborodov A. M., Chomiuk L., Sokoloski J. L., Nelson T., 2014, MNRAS, 442, 713
Metzger B. D., Finzell T., Vurm I., Hascoët R., Beloborodov A. M., Chomiuk L., 2015, MNRAS, 450, 2739
Metzger B. D., Caprioli D., Vurm I., Beloborodov A. M., Bartos I., Vlasov A., 2016, MNRAS, 457, 1786
Metzger B. D., Zenati Y., Chomiuk L., Shen K. J., Strader J., 2021, ApJ, 923, 100
Mezger P. G., Henderson A. P., 1967, ApJ, 147, 471
Moellenbrock G. A. I., 1999, PhD thesis
Mroz P., Burdge K., Roestel J. v., Prince T., Kong A. K. H., Li K. L., 2021, Astron. Telegram, 14720, 1
Mukai K., 2017, PASP, 129, 062001
Mukai K., Sokoloski J. L., 2019, Phys. Today, 72, 38
Mukai K. et al., 2014, in Woudt P. A., Ribeiro V. A. R. M., eds, ASP Conf. Ser. Vol. 490, Stellar Novae: Past and Future Decades. Astron. Soc. Pac., San Francisco, p. 327
Mukai K., Rana V., Bernardini F., de Martino D., 2015, ApJ, 807, L30
Munari U., Zwitter T., 1997, A&A, 318, 269
Munari U., Hambsch F. J., Frigo A., 2017, MNRAS, 469, 4341
Munari U., Valisa P., Dallaporta S., 2021, Astron. Telegram, 14704, 1
Munari U., Giroletti M., Marcote B., O'Brien T. J., Veres P., Yang J., Williams D. R. A., Woudt P., 2022, A&A, 666, L6
Murphy-Glaysher F. J. et al., 2022, MNRAS, 514, 6183
Naito H. et al., 2022, ApJ, 932, 39
Nelson T., Mukai K., Orio M., Luna G. J. M., Sokoloski J. L., 2011, ApJ, 737, 7
Nelson T. et al., 2019, ApJ, 872, 86
Nelson T. et al., 2021, MNRAS, 500, 2798
Ness J. U. et al., 2013, A&A, 559, A50
Norton A. J., Watson M. G., 1989, MNRAS, 237, 853
Norton A. J., Watson M. G., King A. R., 1988, MNRAS, 231, 783
Nyamai M. M., Chomiuk L., Ribeiro V. A. R. M., Woudt P. A., Strader J., Sokolovsky K. V., 2021, MNRAS, 501, 1394
Nyamai M. M., Linford J. D., Allison J. R., Chomiuk L., Woudt P. A., Ribeiro V. A. R. M., Sarbadhicary S. K., 2023, preprint (arXiv:2301.09116)
O'Brien T. J., Lloyd H. M., Bode M. F., 1994, MNRAS, 271, 155
O'Brien T. J. et al., 2006, Nature, 442, 279
Ofek E. O. et al., 2014, ApJ, 788, 154
Orio M., Rana V., Page K. L., Sokoloski J., Harrison F., 2015, MNRAS, 448, L35
Orio M. et al., 2018, ApJ, 862, 164
Orio M. et al., 2020, ApJ, 895, 80
Orio M. et al., 2022a, ApJ, 932, 45
Orio M. et al., 2022b, ApJ, 938, 34
Pacholczyk A. G., 1970, Radio Astrophysics. Nonthermal Processes in Galactic and Extragalactic Sources. Freeman, San Francisco
Paczynski B., 1976, in Eggleton P., Mitton S., Whelan J., eds, Proc. IAU Symp. Vol. 73, Structure and Evolution of Close Binary Systems. Kluwer, Dordrecht, p. 75
Page K. L., Orio M., Sokolovsky K. V., Kuin N. P. M., 2021, Astron. Telegram, 14747, 1
Page K. L., Beardmore A. P., Starrfield S., Wagner R. M., Woodward C. E., 2022, Astron. Telegram, 15317, 1
Pala A. F. et al., 2022, MNRAS, 510, 6110
Paragi Z., Munari U., Yang J., Veres P., Marcote B., Giroletti M., 2021, Astron. Telegram, 14758, 1
Patterson J., 1994, PASP, 106, 209
Patterson J., Epstein-Martin M., Vanmunster T., Kemp J., 2021, Astron. Telegram, 14856, 1
Patterson J. et al., 2022, ApJ, 940, L56
Pei S., Luna G. J. M., Orio M., Behar E., Giese M., Mikolajewska J., Ness J.-U., 2021, Astron. Telegram, 14798, 1

Pejcha O., Metzger B. D., Tomida K., 2016, MNRAS, 461, 2527

Perley R. A., Butler B. J., 2017, ApJS, 230, 7

Perley R. A., Chandler C. J., Butler B. J., Wrobel J. M., 2011, ApJ, 739, L1

Pickering W. H., 1895, Observatory, 18, 436

Piran T., Svirski G., Krolik J., Cheng R. M., Shiokawa H., 2015, ApJ, 806, 164

Poole T. S. et al., 2008, MNRAS, 383, 627

Prialnik D., 1986, ApJ, 310, 222

Proxauf B., Öttl S., Kimeswenger S., 2014, A&A, 561, A10

Quimby R. M., Shafter A. W., Corbett H., 2021, Res. Notes Am. Astron. Soc., 5, 160

Razzaque S., Jean P., Mena O., 2010, Phys. Rev. D, 82, 123012

Readhead A. C. S., 1994, ApJ, 426, 51

Rector T. A. et al., 2022, ApJ, 936, 117

Ribeiro V. A. R. M., Bode M. F., Darnley M. J., Barnsley R. M., Munari U., Harman D. J., 2013, MNRAS, 433, 1991

Ribeiro V. A. R. M. et al., 2014, ApJ, 792, 57

Ritter H., 2010, Mem. Soc. Astron. Ital., 81, 849

Roming P. W. A. et al., 2005, Space Sci. Rev., 120, 95

Rupen M. P., Mioduszewski A. J., Sokoloski J. L., 2008, ApJ, 688, 559

Rybicki G. B., Lightman A. P., 1979, Radiative Processes in Astrophysics. Wiley, New York

Santamaría E., Guerrero M. A., Zavala S., Ramos-Larios G., Toalá J. A., Sabin L., 2022, MNRAS, 512, 2003

Scaringi S., Groot P. J., Knigge C., Lasota J. P., de Martino D., Cavecchi Y., Buckley D. A. H., Camisassa M. E., 2022a, MNRAS, 514, L11

Scaringi S. et al., 2022b, Nature, 604, 447

Schaefer B. E., 2010, ApJS, 187, 275

Schaefer B. E., 2022, MNRAS, 517, 6150

Schaefer G. H. et al., 2020, in Tuthill P. G., Mérand A., Sallum S., eds, Proc. SPIE Conf. Ser. Vol. 11446, Optical and Infrared Interferometry and Imaging VII. SPIE, Bellingham, p. 1144605

Schenker K., Kolb U., Ritter H., 1998, MNRAS, 297, 633

Schmidt R. E., Shugarov S. Y., Afonina M. D., 2021, J. Am. Assoc. Var. Star Obs., 49, 257

Schreiber M. R., Zorotovic M., Wijnen T. P. G., 2016, MNRAS, 455, L16

Schwarz G. J., Shore S. N., Starrfield S., Hauschildt P. H., Della Valle M., Baron E., 2001, MNRAS, 320, 103

Schwarz G. J., Shore S. N., Starrfield S., Vanlandingham K. M., 2007, ApJ, 657, 453

Schwarz G. J. et al., 2011, ApJS, 197, 31

Seaquist E. R., Bode M. F., 2008, in Bode M. F., Evans A., eds, Classical Novae. Cambridge Univ. Press, Cambridge, p. 141

Seaquist E. R., Bode M. F., Frail D. A., Roberts J. A., Evans A., Albinson J. S., 1989, ApJ, 344, 805

Shafter A. W., 2017, ApJ, 834, 196

Shafter A. W., Rau A., Quimby R. M., Kasliwal M. M., Bode M. F., Darnley M. J., Misselt K. A., 2009, ApJ, 690, 1148

Shankar A., Livio M., Truran J. W., 1991, ApJ, 374, 623

Shappee B. J. et al., 2014, ApJ, 788, 48

Shara M. M., 1989, PASP, 101, 5

Shara M. M., Prialnik D., Hillman Y., Kovetz A., 2018, ApJ, 860, 110

Shaviv N. J., 2001, MNRAS, 326, 126

Shaw A. W., Heinke C. O., Mukai K., Sivakoff G. R., Tomsick J. A., Rana V., 2018, MNRAS, 476, 554

Shen K. J., Quataert E., 2022, ApJ, 938, 31

Shepherd M. C., 1997, in Hunt G., Payne H., eds, ASP Conf. Ser. Vol. 125, Astronomical Data Analysis Software and Systems VI. Astron. Soc. Pac., San Francisco, p. 77

Shepherd M. C., Pearson T. J., Taylor G. B., 1994, Bull. Am. Astron. Soc., 987

Shugarov S., Afonina M., 2021, Perem. Zvezdy, 41, 4

Snell R. L., Kurtz S. E., Marr J. M., 2019, Fundamentals of Radio Astronomy: Astrophysics. CRC Press, Boca Raton

Soker N., Livio M., 1989, ApJ, 339, 268

Sokoloski J. L., Rupen M. P., Mioduszewski A. J., 2008, ApJ, 685, L137

Sokolovsky K. V. et al., 2017, MNRAS, 464, 274

Sokolovsky K. V. et al., 2020, MNRAS, 497, 2569

Sokolovsky K. et al., 2021, Astron. Telegram, 14731, 1

Sokolovsky K. V. et al., 2022a, MNRAS, 514, 2239

Sokolovsky K. V. et al., 2022b, ApJ, 934, 142

Sparks W. M., 1969, ApJ, 156, 569

Sparks W. M., Sion E. M., 2021, ApJ, 914, 5

Sparks W. M., Starrfield S., Truran J. W., 1978, ApJ, 220, 1063

Starrfield S., Truran J. W., Sparks W. M., Kutter G. S., 1972, ApJ, 176, 169

Starrfield S., Truran J. W., Sparks W. M., 1978, ApJ, 226, 186

Starrfield S., Iliadis C., Hix W. R., 2016, PASP, 128, 051001

Starrfield S., Bose M., Iliadis C., Hix W. R., Woodward C. E., Wagner R. M., 2020, ApJ, 895, 70

Steinberg E., Metzger B. D., 2018, MNRAS, 479, 687

Stockman H. S., Schmidt G. D., Lamb D. Q., 1988, ApJ, 332, 282

Strope R. J., Schaefer B. E., Henden A. A., 2010, AJ, 140, 34

Sun B., Orio M., Dobrotka A., Luna G. J. M., Shugarov S., Zemko P., 2020, MNRAS, 499, 3006

Takeda L., Diaz M., Campbell R. D., Lyke J. E., Lawrence S. S., Linford J. D., Sokolovsky K. V., 2022, MNRAS, 511, 1591

Tarasova T. N., Skopal A., 2016, Astron. Lett., 42, 10

Taylor A. R., Seaquist E. R., Hollis J. M., Pottasch S. R., 1987, A&A, 183, 38

Taylor A. R., Davis R. J., Porcas R. W., Bode M. F., 1989, MNRAS, 237, 81

ten Brummelaar T. A. et al., 2005, ApJ, 628, 453

Thompson A. R., Clark B. G., Wade C. M., Napier P. J., 1980, ApJS, 44, 151

Thompson A. R., Moran J. M., Swenson G. W. J., 2017, Interferometry and Synthesis in Radio Astronomy, 3rd edn. Springer, Cham

Truran J. W., Livio M., 1986, ApJ, 308, 721

van den Bergh S., Younger P. F., 1987, A&AS, 70, 125

Ueda S. et al., 2021, Central Bureau Electronic Telegrams 4976

Vanlandingham K. M., Starrfield S., Wagner R. M., Shore S. N., Sonneborn G., 1996, MNRAS, 282, 563

Vanlandingham K. M., Schwarz G. J., Shore S. N., Starrfield S., Wagner R. M., 2005, ApJ, 624, 914

Vlasov A., Vurm I., Metzger B. D., 2016, MNRAS, 463, 394

Vogt N., 1990, ApJ, 356, 609

Vurm I., Metzger B. D., 2018, ApJ, 852, 62

Wagner R. M., Woodward C. E., Starrfield S., Banerjee D. P. K., Evans A., 2021, Astron. Telegram, 14746, 1

Walker M. F., 1956, ApJ, 123, 68

Warner B., 1987, MNRAS, 227, 23

Warner B., 2008, Cambridge Univ. Press, Cambridge

Weston J. H. S., 2016, PhD thesis

Weston J. H. S. et al., 2016a, MNRAS, 457, 887

Weston J. H. S. et al., 2016b, MNRAS, 460, 2687

Williams R. E., 1985, European Southern Observatory Conference and Workshop Proceedings. European Southern Observatory, Garching, West Germany, p. 225

Wolf W. M., Bildsten L., Brooks J., Paxton B., 2013, ApJ, 777, 136

Woodward C. E., Banerjee D. P. K., Geballe T. R., Page K. L., Starrfield S., Wagner R. M., 2021, ApJ, 922, L10

Woodward C. E., Wagner R. M., Starrfield S., 2022, Res. Notes Am. Astron. Soc., 6, 124

Yang J., Paragi Z., O'Brien T., Chomiuk L., Linford J. D., 2014, Proceedings of the 12th European VLBI Network Symposium and Users Meeting (EVN 2014). p. 53

Zel'dovich Y. B., Raizer Y. P., 1967, Physics of Shock Waves and High-Temperature Hydrodynamic Phenomena. Academic Press, New York

[1]*Department of Astronomy, University of Illinois at Urbana-Champaign, 1002 W. Green Street, Urbana, IL 61801, USA*

[2]*Department of Physics and Astronomy, Michigan State University, 567 Wilson Road, East Lansing, MI 48824, USA*

[3]*College of Science, George Mason University, Fairfax, VA 22030, USA*

[4]*Lehrstuhl für Astronomie, Universität Würzburg, Emil-Fischer-Street 31, D-Würzburg 97074, Germany*

[5]*CNRS, IRAP, F-31028 Toulouse CEDEX 4, France*

[6]GAHEC, Université de Toulouse, UPS-OMP, IRAP, F-31400 Toulouse, France
[7]Space Science Division, Naval Research Laboratory, Washington, DC 20375-5352, USA
[8]CRESST and X-ray Astrophysics Laboratory, NASA/GSFC, Greenbelt, MD 20771, USA
[9]National Radio Astronomy Observatory, Domenici Science Operations Center, 1003 Lopezville Road, Socorro, NM 87801, USA
[10]National Research Council, Herzberg Astronomy and Astrophysics, 717 White Lake Road, PO Box 248, Penticton, BC V2A 6J9, Canada
[11]Department of Physics and Columbia Astrophysics Laboratory, Columbia University, New York, NY 10027, USA
[12]Racah Institute of Physics, The Hebrew University, 9190401 Jerusalem, Israel
[13]Tartu Observatory, University of Tartu, Tõravere, 61602 Tartumaa, Estonia
[14]Center for Computational Astrophysics, Flatiron Institute, 162 5th Avenue, New York, NY 10010, USA
[15]School of Physics & Astronomy, University of Leicester, Leicester LE1 7RH, UK
[16]Department of Astronomy, University of Wisconsin–Madison, 475 N. Charter Street, Madison, WI 53706, USA
[17]INAF – Padova, vicolo Osservatorio, 5, I-35122 Padova, Italy
[18]Department of Astronomy and Mount Laguna Observatory, San Diego State University, San Diego, CA 92182, USA
[19]Kavli Institute for the Physics and Mathematics of the Universe (WPI), The University of Tokyo Institutes for Advanced Study, The University of Tokyo, Kashiwa, Chiba 277-8583, Japan
[20]Department of Physics and Astronomy, University of North Carolina at Chapel Hill, Chapel Hill, NC 27599-3255, USA
[21]AAVSO Observer
[22]Remote observer of Burke-Gaffney Observatory, Abbey Ridge Observatory and Mini-Robotic Observatory, Canada
[23]School of Physics and Astronomy, Rochester Institute of Technology, 84 Lomb Memorial Drive, Rochester, NY 14623, USA
[24]Center for Backyard Astrophysics Illinois, Northbrook Meadow Observatory, 855 Fair Ln, Northbrook, IL 60062, USA
[25]Center for Backyard Astrophysics Belgium, Walhostraat 1a, B-3401 Landen, Belgium
[26]Center for Backyard Astrophysics Extremadura, e-EyE Astronomical Complex, E-06340 Fregenal de la Sierra, Spain
[27]Burke-Gaffney Observatory, Saint Mary's University, 923 Robie Street, Halifax, NS B3H 3C3, Canada

This paper has been typeset from a TEX/LATEX file prepared by the author.